Master Thesis

Computing Spin-Corrections to the Static Potential using the Multilevel Algorithm

Michael Eichberg

August 2021

Institut für theoretische Physik
Goethe Universität
Franfurt am Main

1. Supervisor:
Prof. Dr. Marc Wagner
Insitut für theoretische Physik
Goethe Universität
Frankfurt a. M.

2. Supervisor:
Prof. Dr. Owe Philipsen
Insitut für theoretische Physik
Goethe Universität
Frankfurt a. M.

Erklärung nach § 30 (12) Ordnung für den Bachelor- und dem Masterstudiengang

Hiermit erkläre ich, dass ich die Arbeit selbstständig und ohne Benutzung anderer als der angegebenen Quellen und Hilfsmittel verfasst habe. Alle Stellen der Arbeit, die wörtlich oder sinngemäß aus Veröffentlichungen oder aus anderen fremden Texten entnommen wurden, sind von mir als solche kenntlich gemacht worden. Ferner erkläre ich, dass die Arbeit nicht - auch nicht auszugsweise - für eine andere Prüfung verwendet wurde.

Frankfurt, den

(Michael Eichberg)

Abstract

Modern studies in hadron spectroscopy using for example the Born-Oppenheimer approximation require accurate descriptions for heavy quark potentials. One type of relativistic corrections are spin-dependent potentials, which cause the fine- and hyperfine splitting in heavy quarkonia spectra. These corrections require colour field correlation functions from lattice computations. Unfortunately, Monte Carlo simulations for these correlation functions suffer from a small signal-to-noise ratio at intermediate and large loop sizes. For Polyakov loops, the multilevel algorithm is already successfully in use and led to significant improvements. In this thesis, we try to reproduce results from reference [1] and investigate the multilevel algorithm for Wilson loops. We found, that the multilevel algorithm leads to a small signal-to-noise ratio and gives access to large quark separations.

Contents

Chapter 1

Introduction

Heavy quark potentials are important for a variety of modern studies, in particular for tetra-quarks and hybrid mesons. These studies rely on accurate descriptions for heavy-quark potentials, which are still not perfectly understood. Early experimental results have shown, that heavy quarks fit into a non-relativistic picture. Soon after the discovery of heavy-quark bound states J/ψ and Υ, the search for relativistic corrections to the static potential has begun. An expansion of the $q\bar{q}$-propagator in powers of the inverse mass has led to corrections connected to spin effects at order $\mathcal{O}(m^{-2})$, which are referred to as the Eichten-Feinberg-Gromes formulae [2, 3]. Velocity-dependent corrections have been derived at this order as well [4]. Later, with the application of potential non-relativistic QCD (pNRQCD), further corrections have been found at $\mathcal{O}(m^{-1})$ [5].

Heavy quark potentials find application in particular in mass spectroscopy, with different methods in use. In the case of systems where both, heavy and light quarks are present, the Born-Oppenheimer approximation finds application. In a system like this, heavy quarks are approximately static in comparison to light quarks, due to the mass difference. This allows to non-relativistic computations, in particular solving the Schrödinger equation for the heavy quarks using heavy quark potentials. In references [6, 7], spectra for systems consisting of bottom quarks and light quarks were computed in the Born-Oppenheimer approximation, using static potentials from lattice QCD. The Born-Oppenheimer approximation can also be used in form of an effective theory, in particular pNRQCD. Here,

one simplifies the computation by integrating out energy scales $\sim m$ (what leads to non-relativistic QCD, or NRQCD) and then $\sim mv$ in form of matching coefficients before solving the Schrödinger equation [8]. Reference [9] applied a combination of the above mentioned relativistic corrections to compute mass spectra of charmonium and bottomonium states in pNRQCD. For both, bottomonium and charmonium states, this significantly increased the accuracy of the results. Thus, relativistic corrections to the static potential appear to be significant contributions for these computations. The full set of the above mentioned relativistic corrections is also promising for computations involving charm quarks.

Relativistic corrections to the static potential can be computed via time integrals over colour-field correlation functions. These correlation functions can be computed numerically, using Monte Carlo methods from lattice QCD. In lattice QCD, the gauge field is represented by so-called link-variables, elements of the group $SU(N)$. Colour field correlators can be constructed via inserting a combination of so-called plaquettes into a closed loop of link-variables and taking the trace. In references [1, 10], results for spin-dependent corrections in $SU(2)$ and $SU(3)$ are presented. A computation of the non-relativistic corrections at $\mathcal{O}(m^{-1})$ is performed in reference [11].

Statistical errors in Monte Carlo simulations scale with the inverse square root of the number of measurements. In the case of spin-dependent corrections to the static quark potential, expectation values are affected by large signal-to-noise ratios [1, 10]. The error increases exponentially with the spatial times temporal length of the loop, or the area covered by a rectangular loop. Generating more configurations to improve errors is not an effective way to face this problem, a better algorithm is needed. The multilevel algorithm aims to improve these errors exponentially. The lattice is separated into several time slices with fixed spatial boundaries. For each time slice, a number of sublattice configurations is generated using a Monte Carlo updating algorithm. The part of an observable on a time slice is averaged over a set of sublattices, after that, the full operator is constructed. Since time slices can be updated independently, the number of sublattice updates increases the total number of measurements in fact exponentially. This causes a more effective improvement of the signal-to-noise ratio [12].

This thesis investigates spin-dependent corrections to the static potential in $SU(2)$ at $\beta = 2.74$, as it was done in reference [1]. We improve the results of reference [1] by applying the multilevel algorithm for Wilson loops. Chapter 2 summarizes the theoretical basics from the references and defines the notation. The main parts are the required correlation functions, the spin-dependent corrections to the potential and the multilevel algorithm. In chapter 3, the results for correlators, as well for the spin-potentials, are presented. The conclusion and outlook for later works are discussed in chapter 4.

Chapter 2

Theoretical Basics

2.1 Observables in Lattice Gauge Theory

2.1.1 Wilson Gauge Action and Wilson Loops

This subsection recaptures the basic ideas behind Wilson loops on the lattice and sets the notation used in this thesis. It is based on reference [13].

In lattice gauge theory, one can compute vacuum expectation values of observables using path integrals. The notation is

$$\langle O \rangle = \frac{1}{Z} \int \mathcal{D}[U] e^{-S_G[U]} O[U] \tag{2.1}$$

where $\mathcal{D}[U]$ is the gauge-invariant Haar-measure, $S_G[U]$ the Wilson gauge action and $O[U]$ the observable. Z is a partition function, which leads to $\langle 1 \rangle \equiv 1$. To find an expression for the action $S_G[U]$, consider a lattice for Yang-Mills theory. The lattice Λ consists of $L_\Lambda^3 \cdot T_\Lambda$ points with so-called link variables $U_\mu(n)$ for each direction $\pm\mu$ attached to each point $n = (n_0, n_1, n_2, n_3)$. $U_\mu(n)$ are elements of the group $SU(N)$. Since gauge fields $A_\mu(x)$ are elements of the algebra to $SU(N)$, one can identify $U_\mu(n) = \exp(ia\hat{A}_\mu(n))$, which shows, that $U_\mu(n)$ in the continuum limit is identical to so-called gauge transporters. As

a consequence, one finds the identity $U_{-\mu}(n) = U_\mu^\dagger(n-\hat{\mu})$. The gauge transformation of $U_\mu(n)$ takes the form

$$U_\mu(n) \to U'_\mu(n) = \Omega(n) U_\mu(n) \Omega^\dagger(n+\hat{\mu}) \tag{2.2}$$

with $\Omega(n) \in SU(N)$. It is clear to see, that for products, the Ω's between two neighbouring U's becomes the identity, i. e. $\Omega(n-\hat{\mu})U_\mu(n-\hat{\mu})\Omega^\dagger(n)\Omega(n)U_\nu(n)\Omega(n+\hat{\nu}) = \Omega(n-\hat{\mu})U_\mu(n-\hat{\mu})U_\nu(n)\Omega(n+\hat{\nu})$. The transformation cancels between the product of two neighbouring link-variables. One can then see, that the trace of the product of link-variables along a closed loop is a gauge invariant quantity. The non-Abelian nature of $SU(N)$ prevents transformation matrices of the left and right side of the product to cancel out. Taking the trace allows to exploit cyclicity. The smallest loop one can construct in this fashion is called a plaquette. The notation is

$$\begin{aligned} U_{\mu\nu}(n) &= U_\mu(n) U_\nu(n+\hat{\mu}) U_\mu^\dagger(n+\hat{\mu}+\hat{\nu}) U_\nu^\dagger(n+\hat{\nu}) \\ &= \exp(ia\hat{A}_\mu(n)) \exp(ia\hat{A}_\nu(n+\hat{\mu})) \exp(-ia\hat{A}_\mu(n+\hat{\mu}+\hat{\nu})) \exp(-ia\hat{A}_\nu(n+\hat{\nu})) \\ &= \exp(ia^2 \hat{F}_{\mu\nu}(n) + \mathcal{O}(a^3)) \end{aligned} \tag{2.3}$$

Note, that we have identified the field strength tensor in the exponential.
Using the plaquette, one can find for the Wilson gauge action

$$\begin{aligned} S_G[U] &= \frac{2}{g^2} \sum_{n\in\Lambda} \sum_{\mu<\nu} \text{Re tr}[\text{id} - U_{\mu\nu}(n)] \\ &= \frac{a^4}{2g^2} \sum_{n\in\Lambda} \sum_{\mu,\nu} \text{tr}[F_{\mu\nu}^2] + \mathcal{O}(a^2) \end{aligned} \tag{2.4}$$

In the continuum limit $a \to 0$, one finds $\lim_{a\to 0} S_G[U] = S_G[A]$. The technicalities of the continuum limit of the Wilson action are elaborated in reference [13].

The Wilson loop is an observable which is commonly used, as it is simple to compute and contains important information. It is a rectangular loop, consisting of two spatial and temporal lines. With $\hat{\mathbf{L}}(n, \mathbf{r}/a)$ denoting a spatial line, starting at lattice point n, in direction $\mathbf{r}/a$ and $\hat{T}(n, t/a)$ denoting a temporal line at n of length t/a, the Wilson loop

can be written as

$$W(n, \mathbf{r}/a, t/a) = \mathrm{tr}[\hat{\mathbf{L}}(n, \mathbf{r}/a)\hat{T}(n + (0, \mathbf{r}/a), t/a)\hat{\mathbf{L}}^{\dagger}(n + t\hat{\mathbf{n}}_0/a, \mathbf{r}/a)\hat{T}^{\dagger}(n, t/a)] \tag{2.5}$$

Bold faces indicate, that the quantity faces into a spatial direction, i. e. has vector-character. When discussing the multilevel algorithm, $\hat{T}(n + (0, \mathbf{r}/a), t/a)_{\alpha\gamma}\hat{T}^{\dagger}(n, t/a)_{\beta\delta}$ (colour indices $\alpha, \beta, \gamma, \delta$) are replaced with the two-link operator $\hat{\mathbf{T}}(n, \mathbf{r}/a, t/a)_{\alpha\beta\gamma\delta}$.
The expectation value $\langle W(\mathbf{r}/a, t/a)\rangle$ of the Wilson loop does not depend on the gauge. Therefore, one can go into temporal gauge, where one can see that the Wilson loop is the correlator between the two spatial lines $\hat{\mathbf{L}}, \hat{\mathbf{L}}^{\dagger}$. The spectral decomposition is

$$\begin{aligned} \langle W(\mathbf{r}/a, t/a)\rangle &= \sum_k |\langle 0|\hat{\mathbf{L}}(\mathbf{r}/a)_{ab}|k\rangle|^2 e^{-(t/a)\hat{E}_k} \\ &\propto e^{-(t/a)\hat{V}(r/a)}(1 + \mathcal{O}(e^{-(t/a)\Delta\hat{E}})) \end{aligned} \tag{2.6}$$

$\hat{\mathbf{L}}(\mathbf{r}/a)$ and $\hat{\mathbf{L}}(\mathbf{r}/a)^{\dagger}$ are the creation and annihilation operators of a quark-antiquark pair with separation $\mathbf{r}/a$ in the static limit. Hence, one identifies $\hat{E}_1 = \hat{V}_0(r/a)$ and $\Delta\hat{E}$ denoting the difference between $\hat{V}_0(r/a)$ and the energy of the next excited state. Lattice quantities, denoted by a hat symbol, are connected to physical quantities via a dimension cancelling factor, e. g. $\hat{V}_0(r/a) = aV_0(r/a)$.

2.2 Spin-dependent Corrections

In systems containing heavy and light quarks, heavy quarks can be seen in a non-relativistic picture. This is used, for example, in the Born-Oppenheimer approximation. Splitting the computation for the heavy and light degrees of freedom, one perform the computation for the heavy quarks using a Schrödinger equation. The standard for computations involving heavy and light quarks was to treat the heavy quarks as static particles, realised with the static potential. Adding relativistic corrections to the static potential is expected to lead to significantly more accurate computations. Examples for computations, which use the static potential and can benefit from these corrections, are references [6, 7]. In context of the Wilson loop formalism, one can derive correction terms to the $q\bar{q}$-potential around

the static limit by expanding the propagator in powers of $1/m$. At order m^{-2}, one can find contributions which are connected to spin-effects. These spin-dependent contributions cause fine- and hyperfine splitting of heavy quarkonia spectra [2].
We will briefly sketch, how one can expand the quark propagator in terms of m^{-1}. Seeing the propagator $S(x, y; A)$ as the Green's function to the Dirac equation

$$(\gamma^\mu D_\mu - m)S(x, y; A) = \delta^4(x - y) \tag{2.7}$$

with covariant derivative $D_\mu = i\partial_\mu + gA_\mu$, its non-relativistic counterpart is defined via

$$(\gamma^0 D_0 - m)S_0(x, y; A) = \delta(x_0 - y_0) \tag{2.8}$$

for which the formal solution is proportional to $e^{-m(x^0-y^0)}$ can be found in reference [2]. From this, one can construct an integral equation for $S(x, y; A)$:

$$S(x, y; \mathbf{A}) = S_0(x, y; \mathbf{A}) + \int d^4z S(x, z; \mathbf{A})\vec{\gamma}\mathbf{D}S(z, y; A) \tag{2.9}$$

One can simplify the problem with projection operators $\mathcal{P}^\pm = \frac{1\pm\gamma^0}{2}$, i. e. writing the equation in terms of $S^{ab}(x, y; A) = \mathcal{P}^a S(x, y; A)\mathcal{P}^b$, $a, b = +, -$. This results in

$$S^{++}(x, y; A) = S_0^{++}(x, y; A) + \int d^4z d^4w S_0^{++}(x, z; A)\vec{\gamma}\mathbf{D}S_0^{--}(z, w; A)\vec{\gamma}\mathbf{D}S^{++}(w, y; A) \tag{2.10}$$

Equation (2.10) has an intuitive interpretation, the Feynman graph can be seen in figure (2.1). The first term describes a particle propagating from x to y, only interacting non-relativistically with the gauge field. In the second term, the particle propagates to z first, where it scatters with the interaction kernel $\vec{\gamma}\mathbf{D}$ and travels backwards to point w. Both propagations again include solely non-relativistic interactions. At point w, it scatters again, this time propagating forward to y and interacting fully relativistically. One can plug the full solution of S_0 into this equation and perform integration by parts for the time components. Each integration by parts takes the remaining integral to a higher order in m^{-1}. The full derivation of all terms proportional to m^{-2}, as well as a scheme for higher orders, is performed in reference [2].

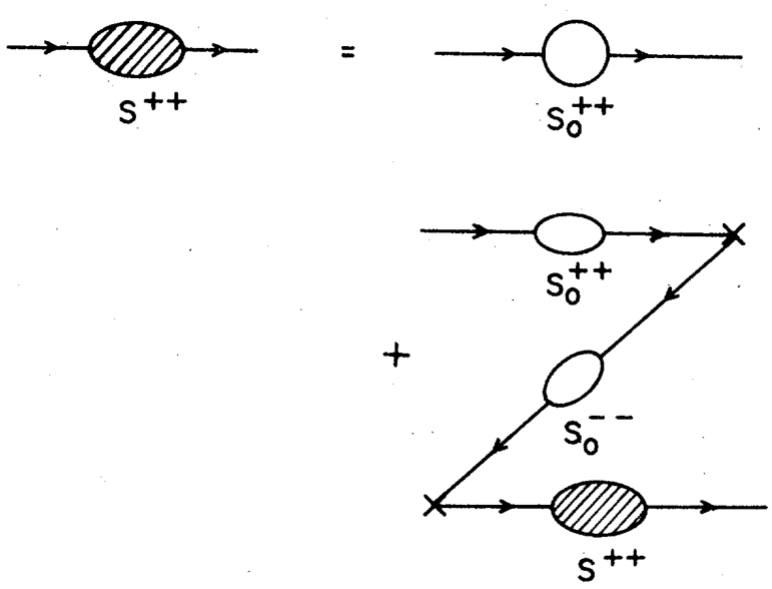

Figure 2.1: Feynman graph to equation (2.10), taken from reference [2].

The computation of the spin-dependent correction terms can be performed in a formalism which uses Wilson loops in the non-relativistic limit. In short, one can write the Wilson loop expectation value in the continuum in terms of quark propagators $S(x, y; A)$. By substituting $S(x, y; A)$ with the static propagator $S_0(x, y; A)$, one can find an expression for the potential in the static limit. Likewise, one can instead insert an expansion of $S_0(x, y; A)$ up to arbitrary power in m^{-1}, in order to find an expression for relativistic corrections to the static potential. Reference [2] presented this computation for spin-dependent corrections in detail. For heavy quark masses M_1, M_2, one can write spin-dependent contributions as

$$\begin{aligned} V_{\mathrm{sd}}(r; \mathbf{L}, \mathbf{S}_1, \mathbf{S}_2) = & \left(\frac{\mathbf{L}\mathbf{S}_1}{M_1^2} + \frac{\mathbf{L}\mathbf{S}_2}{M_2^2} \right) \frac{V_0'(r) + 2V_1'(r)}{2r} \\ & + \frac{\mathbf{L}(\mathbf{S}_1 + \mathbf{S}_2)}{M_1 M_2} \frac{V_2'(r)}{r} \\ & + \left(\frac{(\mathbf{S}_1 \hat{\mathbf{r}})(\mathbf{S}_2 \hat{\mathbf{r}})}{M_1 M_2} - \frac{\mathbf{S}_1 \mathbf{S}_2}{3 M_1 M_2} \right) V_3(r) \\ & + \frac{\mathbf{S}_1 \mathbf{S}_2}{M_1 M_2} V_4(r) \end{aligned} \tag{2.11}$$

with spin-potentials $V_1'(r)$, $V_2'(r)$, $V_3(r)$ and $V_4(r)$ which only depend on the quark separation r. Equation (2.11) can also be defined in the context of an effective field theory framework, such as NRQCD or pNRQCD, with the corresponding matching coefficients

[10]. The spin-potentials can be determined from colour field correlation functions. For colour fields $\hat{\mathbf{E}}$ and $\hat{\mathbf{B}}$, the spin-potentials can be expressed in lattice units as

$$\frac{r_k}{r}\hat{V}_1'(r) = \varepsilon_{ijk}\lim_{\tau\to\infty}\int_0^\tau dt\ t\langle\langle\hat{B}_i(\mathbf{r}_1,t_1)\hat{E}_j(\mathbf{r}_1,t_2)\rangle\rangle \tag{2.12}$$

$$\frac{r_k}{r}\hat{V}_2'(r) = \varepsilon_{ijk}\lim_{\tau\to\infty}\int_0^\tau dt\ t\langle\langle\hat{B}_i(\mathbf{r}_1,t_1)\hat{E}_j(\mathbf{r}_2,t_2)\rangle\rangle \tag{2.13}$$

$$(\frac{r_i r_j}{r^2} - \frac{\delta_{ij}}{3})\hat{V}_3(r) + \frac{\delta_{ij}}{3}\hat{V}_4(r) = 2\lim_{\tau\to\infty}\int_0^\tau dt\ \langle\langle\hat{B}_i(\mathbf{r}_1,t_1)\hat{B}_j(\mathbf{r}_2,t_2)\rangle\rangle \tag{2.14}$$

where $t = t_2 - t_1$ and $\mathbf{r} = \mathbf{r}_2 - \mathbf{r}_1$. t_1, t_2 refer to the temporal and $\mathbf{r}_1, \mathbf{r}_2$ to the spatial 'start' and 'end' of the loop. V_1' and V_2' describe spin-orbit interactions, while V_3 and V_4 correspond to spin-spin interactions. Equations (2.12) to (2.14) can be considerably simplified by choosing $\mathbf{r} \equiv (0,0,r)$. Then, $\frac{r_i r_j}{r^2} = \delta_{ij}$, $\frac{r_k}{r} = \delta_{3k}$ and $\varepsilon_{ij3}B_iE_j = B_1E_2 - B_2E_1$. For the correlators, one can also find for $\mathbf{r} = (0,0,r)$ the relations

$$\langle\langle\hat{B}_1(0,0)\hat{E}_2(0,t)\rangle\rangle = -\langle\langle\hat{B}_2(0,0)\hat{E}_1(0,t)\rangle\rangle \tag{2.15}$$

$$\langle\langle\hat{B}_1(0,0)\hat{E}_2(\mathbf{r},t)\rangle\rangle = -\langle\langle\hat{B}_2(0,0)\hat{E}_1(\mathbf{r},t)\rangle\rangle \tag{2.16}$$

$$\langle\langle\hat{B}_1(0,0)\hat{B}_1(\mathbf{r},t)\rangle\rangle = \langle\langle\hat{B}_2(0,0)\hat{B}_2(\mathbf{r},t)\rangle\rangle \tag{2.17}$$

Using this, the spin-potentials become

$$\hat{V}_1'(r) = 2\lim_{\tau\to\infty}\int_0^\tau dt\ t\langle\langle\hat{B}_1(0,0)\hat{E}_2(0,t)\rangle\rangle \tag{2.18}$$

$$\hat{V}_2'(r) = 2\lim_{\tau\to\infty}\int_0^\tau dt\ t\langle\langle\hat{B}_1(0,0)\hat{E}_2(\mathbf{r},t)\rangle\rangle \tag{2.19}$$

$$\hat{V}_3(r) = 2\lim_{\tau\to\infty}\int_0^\tau dt\langle\hat{B}_3(0,0)\hat{B}_3(t,\mathbf{r})\rangle\rangle - \langle\hat{B}_1(0,0)\hat{B}_1(t,\mathbf{r})\rangle\rangle \tag{2.20}$$

$$\hat{V}_4(r) = 2\lim_{\tau\to\infty}\int_0^\tau dt2\langle\hat{B}_1(0,0)\hat{B}_1(t,\mathbf{r})\rangle\rangle + \langle\hat{B}_3(0,0)\hat{B}_3(t,\mathbf{r})\rangle\rangle \tag{2.21}$$

Making use of the spectral representation of correlators $\langle\langle\hat{F}_1(0)\hat{F}_2(t)\rangle\rangle$, one can integrate analytically. A necessary assumption is, that one can approximate the spectral decomposition for $\langle\langle\hat{F}_1(0)\hat{F}_2(t)\rangle\rangle$ in equation (2.45) with $\sum_m D_m^{12}e^{-\Delta\hat{V}_m t} \approx \sum_{m=0}^{m_{\max}}\tilde{D}^{12}e^{-\Delta\tilde{V}_m t}$ (see

reference [1]). In this case, one finds

$$\begin{aligned}\int_0^\infty dt\ t\langle\langle \hat{F}_1(0)\hat{F}_2(t)\rangle\rangle &\approx \int_0^\infty dt\ t \sum_{m=1}^{m_{\max}} \tilde{D}_m^{12} e^{-\Delta\tilde{V}_m t} \\ &= \sum_{m=1}^{m_{\max}} \int_0^\infty dt\ t\tilde{D}_m^{12} e^{-\Delta\tilde{V}_m t} \\ &= \sum_{m=1}^{m_{\max}} \frac{\tilde{D}_m^{12}}{(\Delta\tilde{V}_m)^2} \end{aligned} \tag{2.22}$$

$$\begin{aligned}\int_0^\infty dt\langle\langle \hat{F}_1(0)\hat{F}_2(t)\rangle\rangle &\approx \int_0^\infty dt \sum_{m=1}^{m_{\max}} \tilde{D}_m^{12} e^{-\Delta\tilde{V}_m t} \\ &= \sum_{m=1}^{m_{\max}} \int_0^\infty dt\tilde{D}_m^{12} e^{-\Delta\tilde{V}_m t} \\ &= \sum_{m=1}^{m_{\max}} \frac{\tilde{D}_m^{12}}{\Delta\tilde{V}_m} \end{aligned} \tag{2.23}$$

Reference [1] argues, that $D_0^{12} = 0$ and as a consequence, all correlation functions decay exponentially. The arguments for this are, that included operators project onto spaces which are orthogonal to each other. Therefore, the sums start at $m = 1$. Additionally, for V_1' and V_2', one finds by demanding invariance under time inversion, that $\sum_m \tilde{D}_m^{12} = 0$. The coefficients $\tilde{D}_m^{12}$ and $\Delta\tilde{V}_m$ can be extracted from fit curves to the lattice data.

The functions for the spin-potentials are related to each other and to the static potential V_0. An exact relation $V_2'(r) - V_1'(r) = V_0'(r)$ was derived by Gromes, by demanding invariance under Lorentz transformations. Reference [10] lists the expected compositions of the spin-potentials in terms of interaction kernels (see table (**??**)). These contributions are later useful to determine and discuss suitable parametrizations for each spin-potential. Vice versa, the quality of the fit curves might give hints to whether the underlying assumptions to the interaction types are correct. If V_1' has a purely scalar interaction kernel and if pseudo-scalar contributions can be neglected for each spin-potential, one finds [1]

$$V_3(r) = \frac{V_2'(r)}{r} - V_2''(r) \tag{2.24}$$

$$V_4(r) = 2\nabla^2 V_2'(r) \tag{2.25}$$

Tree-level results from perturbation theory, combined with the non-perturbative linear contribution, are

$$V_0(r) = -\frac{C_F \alpha_s}{r} + \kappa r \tag{2.26}$$

$$V_1'(r) = -\kappa \tag{2.27}$$

$$V_2'(r) = \frac{C_F \alpha_s}{r^2} \tag{2.28}$$

$$V_3(r) = \frac{3 C_F \alpha_s}{r^3} \tag{2.29}$$

$$V_4(r) = 8\pi\delta^3(r) \tag{2.30}$$

We want to emphasize, that there are more known corrections to the static potential, than the spin-dependent corrections. At order $\mathcal{O}(m^{-1})$, a correction term appears, which is linked to self-interactions of gluons, i. e. three-gluon vertices [9]. At order $\mathcal{O}(m^{-2})$, one finds not only spin-spin and spin-orbit interactions, but also corrections corresponding orbit-orbit interactions [1, 10, 14, 9]. All these corrections are important parts for an accurate description of systems containing heavy quarks.

2.3 Colour Field Correlators

Similar to electric and magnetic fields in electrodynamics, one defines colour fields in $SU(N)$ using the field strength tensor

$$E_i = F_{0i} \tag{2.31}$$

$$B_i = \varepsilon_{ijk} F_{jk} \tag{2.32}$$

Equation (2.3) shows us, that colour fields can be constructed on the lattice using combinations of plaquettes. The so-called clover definition of colour fields uses the following

combinations:

$$\hat{F}_{\mu\nu}(n) = \frac{1}{2i}(\hat{U}_{\mu\nu}(n) - \hat{U}^{\dagger}_{\mu\nu}(n)) \tag{2.33}$$

$$\hat{E}_i(n) = \frac{1}{2}(\hat{F}_{0i}(n) + \hat{F}_{-i0}(n)) \tag{2.34}$$

$$\hat{B}_i(n) = \frac{1}{8}\varepsilon_{ijk}(\hat{F}_{jk}(n) + \hat{F}_{k-j}(n) + \hat{F}_{-k-j}(n) + \hat{F}_{-kj}(n)) \tag{2.35}$$

$\hat{F}_{\mu\nu}, \hat{E}_i, \hat{B}_i$ are the dimensionless lattice counterparts to $F_{\mu\nu}, E_i, B_i$ from the continuum. One might notice here, that the electric field is defined in Euclidean space and is connected to the Minkowski definition via a factor i. To form a correlation function, $\hat{E}$ and $\hat{B}$ can be inserted into the temporal lines of a Wilson loop of temporal size t_W. For purposes which become clear later, colour fields should be inserted 'far' from the spatial lines of the loop. The smallest temporal distance between a field and a spatial line will be denoted by Δt in the following. For a single colour field, one would place it in the center of a temporal line and let $t_W \to \infty$. To avoid effects coming from the finite temporal lattice size, t_W should be smaller than $T_\Lambda/2$ and T_Λ sufficiently large. One can now construct the correlator between two colour fields $\hat{F}_1(0), \hat{F}_2(t/a)$ at times 0 and t/a ($\hat{F}_{1,2}$ can both be either a $\hat{E}$- or a $\hat{B}$-field). Inside a Wilson loop with $t_W = t + 2\Delta t$, we place $\hat{F}_1, \hat{F}_2$ inside the temporal lines and include it in the path ordering. To make formulas more readable, the lattice spacing a will be omitted in the following. In other words, $t = t/a$ and $\mathbf{r} = \mathbf{r}/a$. For $\hat{F}_1(0)$ at $(n_0 + \Delta t, \mathbf{n})$ and $\hat{F}_2(t)$ at $(n_0 + t + \Delta t, \mathbf{n} + \mathbf{r})$ this reads as

$$\begin{aligned}\langle \hat{F}_1(0)\hat{F}_2(t)\rangle_W = \langle \mathrm{tr}[&\hat{\mathbf{\Gamma}}(n,\mathbf{r})\hat{T}(n + (0,\mathbf{r}), \Delta t)\hat{F}_1(n + (\Delta t, \mathbf{r})) \\ &\times \hat{T}(n + (\Delta t, \mathbf{r}), t + \Delta t)\hat{\mathbf{\Gamma}}^{\dagger}(n + (t + 2\Delta t)\hat{n}_0, \mathbf{r}) \\ &\times \hat{T}^{\dagger}(n + (\Delta t + t)\hat{n}_0, \Delta t)\hat{F}_2(n + (t + \Delta t)\hat{n}_0)\hat{T}^{\dagger}(n, t + \Delta t)]\rangle\end{aligned} \tag{2.36}$$

A graphic for equation (2.36) is given in figure (2.2). Here, $\hat{F}_1(0)$ is connected to the lower Wilson line via a temporal line of length Δt and to the upper Wilson line via a temporal line of length $t + \Delta t$. Depending on the notation, one might need $\hat{F}^{\dagger}$ in the loop, or switch the spatial positions. However, as seen from equation (2.33), this only changes the sign of

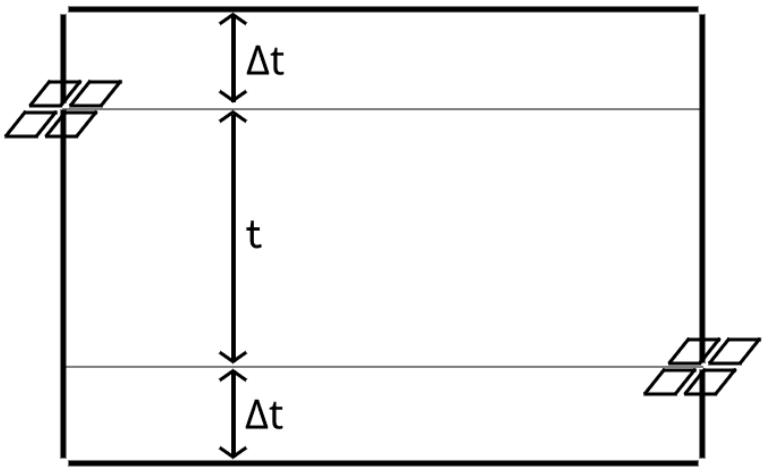

Figure 2.2: Schematic picture of a correlation function, as it is given in equation (2.36). The small rectangles represent the insertions $\hat{F}_1$, $\hat{F}_2$.

the operator. Finally, one divides $\langle \hat{F}_1(0)\hat{F}_2(t)\rangle_W$ by a plain loop:

$$\langle\langle \hat{F}_1(0)\hat{F}_2(t)\rangle\rangle = \frac{\langle \hat{F}_1(0)\hat{F}_2(t)\rangle_W}{\langle W\rangle} \tag{2.37}$$

In the following, $\langle\langle ...\rangle\rangle_W$ denotes $\langle ...\rangle_W / \langle W\rangle$.

The lattice formulation of colour field correlators contains discretization errors, for which renormalization has to be applied. A commonly used renormalization procedure is the one by Huntley and Michael. It uses $\bar{F}_{\mu\nu} = \frac{1}{2}(\hat{U}_{\mu\nu} + \hat{U}^{\dagger}_{\mu\nu})$ to define $\bar{E}_i$ and $\bar{B}_i$ analogue to equations (2.34,2.35). The procedure is perturbatively derived, so lattice artefacts will not entirely be removed. For each colour field $\hat{F}$, one applies a factor of $Z_{\bar{F}} = 1/\langle\langle \bar{F}\rangle\rangle$ multiplicatively. In the case of colour-field correlators, one has

$$\langle\langle \hat{F}_1(0)\hat{F}_2(t)\rangle\rangle = \frac{\langle \hat{F}_1(0)\hat{F}_2(t)\rangle_W \langle W\rangle}{\langle \bar{F}_1\rangle_W \langle \bar{F}_2\rangle_W} \tag{2.38}$$

The quantity $\langle\langle\cdot\rangle\rangle$ can be also computed in the context of other loop structures, with similar results in the limit $t \to \infty$. Reference [10] for instance uses Polyakov loops.

Later analysis will require a suitable parametrization for colour field correlators. Reference

[1] computed the spectral representation

$$\langle\langle \hat{F}_1 \hat{F}_2 \rangle\rangle_W = \sum_m D_m^{12} e^{-\Delta \hat{V}_m t} \times (1 + E_m^{12} e^{-\Delta \hat{V}_1 \Delta t} + ...) \tag{2.39}$$

$$D_m^{12} = \frac{\mathrm{Re}(f_{0m}^1 f_{m0}^2)}{g_{00}^1 g_{00}^2} \tag{2.40}$$

$$E_m^{12} = \frac{\mathrm{Re}[(d_1/d_0)(f_{1m}^1 f_{m0}^2 + f_{0m}^1 f_{m1}^2)]}{\mathrm{Re}(f_{0m}^1 f_{m0}^2)} - \frac{\mathrm{Re}[(d_1/d_0) g_{10}^1]}{g_{00}^1} - \frac{\mathrm{Re}[(d_1/d_0) g_{10}^2]}{g_{00}^2} \tag{2.41}$$

$$d_m = \langle 0 | \hat{\mathbf{\Gamma}}(\mathbf{r}) | m, \mathbf{r} \rangle \tag{2.42}$$

$$f_{mn}^i = \langle m, \mathbf{r} | \hat{F}_i | n, \mathbf{r} \rangle \tag{2.43}$$

$$g_{mn}^i = \langle m, \mathbf{r} | \bar{F}_i | n, \mathbf{r} \rangle \tag{2.44}$$

Where $|0\rangle$ is the ground state of the vacuum and $|n, \mathbf{r}\rangle$ the nth eigenstate of a $q\bar{q}$-pair with separation $\mathbf{r}$. One can see, that a large Δt and a small E_m^{12} allow to approximate

$$\langle\langle \hat{F}_1 \hat{F}_2 \rangle\rangle_W \approx \sum_m D_m^{12} e^{-\Delta \hat{V}_m t} \tag{2.45}$$

2.4 Multilevel Algorithm

This section focuses on the idea behind the multilevel algorithm and the way it is implemented in praxis. It is based on reference [12], which first introduced the method. Wilson loops, as well as Polyakov loops, are computed as statistical expectation values. From a Monte Carlo simulation, where one generates a set of lattice configurations from random numbers, the expectation value is approximated via the mean value of the N measurements. To reduce errors, a straight-forward method would be to increase the statistics, as errors scale with $1/\sqrt{N}$. On the other side, relative errors of Wilson loops scale exponentially with rt for long distances, so the approach to simply increase N will fail eventually for large loop sizes. One example are colour field correlators, used to com-

pute spin-dependent corrections to the static potential. The signal-to-noise ratio can be several magnitudes smaller for colour field correlators than for Wilson loops.

The multilevel algorithm splits operators on the lattice into time slices [1]. For those time slices, one generates a number of so-called sublattices and computes averages.

A loop on the lattice can be separated into slices along the temporal axis as follows. For a Wilson loop, a spatial line can be written in (colour-)index-notation:

$$\mathbf{L}(x_0)_{\alpha\beta} = \{U_i(x) \cdot ... \cdot U_i(x + (r-a)\hat{n}_i)\}_{\alpha\beta} \tag{2.46}$$

with $x = (x_0, a\hat{\mathbf{n}}_i)$. In temporal direction, a so-called two-link operator can be defined as

$$\mathbf{T}(x_0)_{\alpha\beta\gamma\delta} = U_0(x)^*_{\alpha\beta} U_0(x + a\hat{n}_i)_{\gamma\delta} \tag{2.47}$$

Multiplication of two-link operators then takes the form

$$\{\mathbf{T}(x_0)\mathbf{T}(x_0 + a)\}_{\alpha\beta\gamma\delta} = \mathbf{T}(x_0)_{\alpha\lambda\gamma\epsilon}\mathbf{T}(x_0 + a)_{\lambda\beta\epsilon\delta} \tag{2.48}$$

and Wilson loops become

$$W(\mathcal{C}) = \mathbf{L}(0)_{\alpha\gamma}\{\mathbf{T}(0) \cdot ... \cdot \mathbf{T}(t-a)\}_{\alpha\beta\gamma\delta}\mathbf{L}(t)^*_{\beta\delta} \tag{2.49}$$

Monte Carlo updates using the Wilson action (2.4) are performed locally. The locality of the action can be exploited, to define a substructures of the lattice and simulate it independently. Along the temporal axis, the lattice can be split into time slices of variable thickness. Spatial hypercubes on the boundaries between time slices are held fixed. Between boundaries, the gauge links are dynamical degrees of freedom. The whole structure is called the sublattice.

In the two-link operator notation, a loop can be decomposed, such that its parts fit into the time-slices. The locality of the plaquette allows now to perform Monte Carlo updates of the sublattice and take the sublattice average of two-link operators. For time-slices with

[1] Be aware that reference [12] and [10] refer to different quantities, when they say sublattice and time slice. Here, the definition from reference [12] is taken, where a time slice consists of the lattice points in the time interval $[x_0, y_0]$, whereas reference [10] calls this the sublattice.

thickness 1, a sublattice average, denoted by [...], takes the form

$$[\mathbf{T}(x_0)...\mathbf{T}(x_0+t/a-1)] = \frac{1}{Z_{\text{sub}}}\int D[U]_{\text{sub}}\mathbf{T}(x_0)...\mathbf{T}(x_0+t/a-1)e^{-S_G[U]_{\text{sub}}} \tag{2.50}$$

As for operators on the whole lattice, Z_{sub} is the partition function, such that $[1] = 1$. Note, that sublattice expectation values are well-defined objects of link variables on a time-slice with its boundaries, but the respective regions do not depend on each other.
With the global configuration on the top level and a sublattice on the next level, one can substitute two-link operators with their sublattice expectation values

$$\langle W\rangle = \langle \mathbf{L}(0)_{\alpha\gamma}\{[\mathbf{T}(0)...\mathbf{T}(t-a)]\}_{\alpha\beta\gamma\delta}\mathbf{L}^*_{\beta\delta}\rangle \tag{2.51}$$

This scheme can be taken to further levels. If the time slice thicknesses of the sublattice are large, another sublattice can be defined on the next lower level. As an example, a time slice of thickness 2 can fit two time slices of thickness 1. The corresponding expectation values then satisfy the identity

$$[\mathbf{T}(x_0)\mathbf{T}(x_0+a)] = [[\mathbf{T}(x_0)][\mathbf{T}(x_0+a)]] \tag{2.52}$$

As long as time slices on lower levels fit into those of the higher level, time slice patterns can be almost arbitrary. However, one might find exceptions, where thin time-slices can cause problems (see discussion on confinement in reference [12]).

2.4.1 Exactness of the stochastic Mean Value

This section recaptures arguments for the exactness of lattice expectation values computed with the multilevel algorithm, as it is presented in reference [12]. It also pictures, how the algorithm reduces statistical errors.
Assume a system S with a finite number of states $s \in S$, where every s can be written as a vector $(s_0, ..., s_n)$. For simplification, let $s_0, ..., s_n$ be discrete variables. A state $s \in S$

has a stochastic weight $p(s)$, which can be factored as

$$p(s) = p_0(s_0) \prod_{k=1}^{n} p_k(s_0, s_k) \tag{2.53}$$

with

$$\sum_{s_0} p_0(s_0) = 1 = \sum_{s_k} p_k(s_0, s_k) \tag{2.54}$$

$p_0(s_0)$ is the probability, to find the value s_0 in the 0th entry of s. $p_k(s_0, s_k)$ is the probability to find the value s_k in the kth entry, given s_0. For a lattice with two levels (global and one lower level), s_0 relates to the fixed boundaries between time slices on the lower level, while s_k's are the dynamic degrees of freedom. An observable measured in a state s factors as

$$\mathcal{O}(s) = \mathcal{O}_0(s_0) \prod_{k=1}^{n} \mathcal{O}_k(s_0, s_k) \tag{2.55}$$

and one can write the expectation value

$$\langle \mathcal{O} \rangle = \sum_{s_0} p_0(s_0) \mathcal{O}_0(s_0) \prod_{k=1}^{n} [\mathcal{O}_k](s_0), \tag{2.56}$$

$$[\mathcal{O}_k](s_0) = \sum_{s_k} p_k(s_0, s_k) \mathcal{O}_k(s_0, s_k) \tag{2.57}$$

One can show, that mean values computed via the multilevel algorithm, are indeed described by this factorization. A proof is given in reference [12]. The factorization of the mean value of an observable hints on how the application of the multilevel algorithm improves statistical errors. $s_1, ..., s_n$, which are the areas between the fixed time slice boundaries, are updated independently from each other at a given s_0. As a consequence, the conditional probability $p_k(s_0, s_k)$ distribution is simulated. The $N^{(0)}$ updates on the global configuration, as well as the sequence of $N^{(0)}$ global updates and $N^{(1)}$ sublattice updates, simulate $p(s)$. A closer look to the sublattice reveals, that the algorithm actually performs $(N^{(1)})^n$ updates on the sublattice. This is because the n areas between the boundaries do not depend on each other and updates are performed separately.

Chapter 3

Results

For this thesis, we investigated a lattice with parameters given in table 3.1. Further lattice spacings were not investigated.

For the Monte Carlo simulations, C++ programs provided by Christian Reisinger were used to generate gauge field configurations and compute correlation functions with the multilevel algorithm. The multilevel program takes a file, in which structure of the sublattice for every correlator is defined, i. e. how the full lattice is split into time slices. A composition for every two-point function at every t of interest has to be found. This made the search for suitable compositions more complicated and, especially for odd t, compromises had to be made. As an example, a lattice with $T/a = 32$ would fit 32 time-slices of thickness 1. Unfortunately, the program does not allow us to place an $\hat{E}$-field at the edges of a time-slice, since in the clover definition, gauge links from the upper and the lower time slice are needed. This limits the options significantly. Mean values from multilevel computations were found to be equal to conventional computations within errors.
The evaluation of results from the Monte Carlo simulation was performed with Python.

Table 3.1: Parameters for the investigated lattice. The lattice spacing a is taken from reference [1].

Inverse coupling β	Volume $(T/a) \cdot (L/a)^3$	Lattice spacing a [fm]	Spatial size L [fm]	# Configs $N_c^{(0)}$
2.74	$32 \cdot 32^3$	0.041	1.30	1000

For error estimates, a script which uses the single-elimination Jackknife method according to reference [15] was written. Fit parameters for curves were computed via the function `curve_fit` from the library Scipy.

3.1 Multilevel and APE-Smearing Parameters

To optimize multilevel and smearing parameters, $N_c^{(0)} = 100$ thermalized, independent lattice configurations were used. We were looking for sets of multilevel parameters, which minimize the quantity $\sigma^2\tau$, i. e. the square of the standard deviation times the computation time. The investigation of multilevel parameters can be very time consuming. Therefore, in some cases, the set of multilevel parameters was only crudely determined. Nevertheless, we found parameters which were very effective and an improvement to conventional methods.

Previous computations by Christian Reisinger found for the used lattice parameters, that the optimal time slice thickness is about one lattice spacing. The study for $SU(3)$ can be found in reference [16], for $SU(2)$, results were similar. Time slice thickness of two lattice spacings was preferred in this study, since it did not significantly affect results, but led to more convenient sublattice compositions. For Correlators at uneven t/a, we replaced several time slices of thickness 2 with time slices of thickness 3, which led to a reduced number of positions in the lattice on which we could evaluate the correlator. With a fixed sublattice composition using two levels, the only parameters to optimize are the number of sublattice measurements $N_c^{(1)}$ and number of Monte Carlo updates $N_{\text{iupd}}^{(1)}$ in between. $N_{\text{iupd}}^{(0)}$ is conventionally chosen large, such that the correlation between measurements on global configurations is as small as possible. On a sublattice however, $N_{\text{iupd}}^{(1)}$ can be small, compared to $N_{\text{iupd}}^{(0)}$, since the correlation between sublattice measurements is not relevant, if global configurations are uncorrelated. We start the multilevel parameter optimization with $N_{\text{iupd}}^{(0)}$. For fixed $N_c^{(0)}, N_c^{(1)}$, a correlation function was evaluated for different values of $N_{\text{iupd}}^{(1)}$ and search for a minimum in $\sigma^2\tau$. This was the case for $N_{\text{iupd}}^{(1)} = 10$. To optimize $N_c^{(1)}$, $N_c^{(0)}, N_{\text{iupd}}^{(1)}$ were then held fixed and one tries to find the minimum of $\sigma^2\tau$. We found the minimum for correlators at even times and intermediate distances up to $r/a = 7$

Table 3.2: Multilevel parameters used for all correlators for various r and t. The number of evaluated N_{tsl} refers to the number of time slices on the sublattice on which we were able to compute a correlator.

r/a	t/a	#Evaluated N_{tsl}	$N_c^{(1)}$	$N_{\text{iupd}}^{(0)}$
$2-7$	even	16	40	10
$2-7$	odd	4	120	10
$8-10$	even	16	120	10
$8-10$	odd	4	360	10

to be at $N_c^{(1)} = 40$. For the investigated correlators at $r/a = 10$, a minimum was not found up to $N_c^{(1)} \approx 160$. Instead, $\sigma^2\tau$ had a flat slope with only a very small difference between $N_c^{(1)} = 100$ and $N_c^{(1)} = 160$. Due to time limits, we had to restrict $N_c^{(1)}$ to 120 measurements. Nevertheless, the computation was in total significantly more effective than conventional computations. Correlators at uneven t/a could crudely be optimized by tripling $N_c^{(1)}$. The parameters are shown in table 3.2.

An APE-smearing step is the substitution

$$U_i(n) \to \mathcal{P}_{\text{SU(N)}}\Big((1-\alpha_{\text{APE}})U_i(n) + \alpha_{\text{APE}} \sum_{\substack{j=\pm1,\pm2,\pm3 \\ j\neq i}} U_j(n)U_i(n+\hat{n}_j)U_j^\dagger(n+\hat{n}_i)\Big) \quad (3.1)$$

for link-variables in all spatial hypercubes on the lattice with projection on $SU(N)$ $\mathcal{P}_{\text{SU(N)}}$ and a free parameter α_{APE} (here chosen as $\alpha_{\text{APE}} = 0.5$). One can perform this step recursively for N_{APE} iterations. APE smearing is used to increase the overlap between the ground state of a $q\bar{q}$-pair and the vacuum. This is important to the spectral decomposition of both, Wilson loops in equation (2.6) and colour field correlators in equation (2.39), in order to suppress excited states. The investigated colour field correlation functions use Wilson loops with shortest temporal size of $t_W = 6$. The effective static potential is plotted for various numbers of APE-smearing steps. For $r/a = 10$, $V_{\text{eff}}(t/a)$ is shown in figure (3.1). $N_{\text{APE}} = 200$ seemed to be the appropriate choice.

Table 3.3: Fitparameters for $V_0(r)$

	aV_c	c_1	$a^{-1}c_2$	$a^2\kappa$	χ^2/N_{DF}
Conventional	0.48(73)	0.22(78)	0.03(5)	0.0078(15)	0.99
Multilevel	0.489(6)	0.254(5)	0.02(0)	0.00784(0)	0.05

3.2 Static Potential

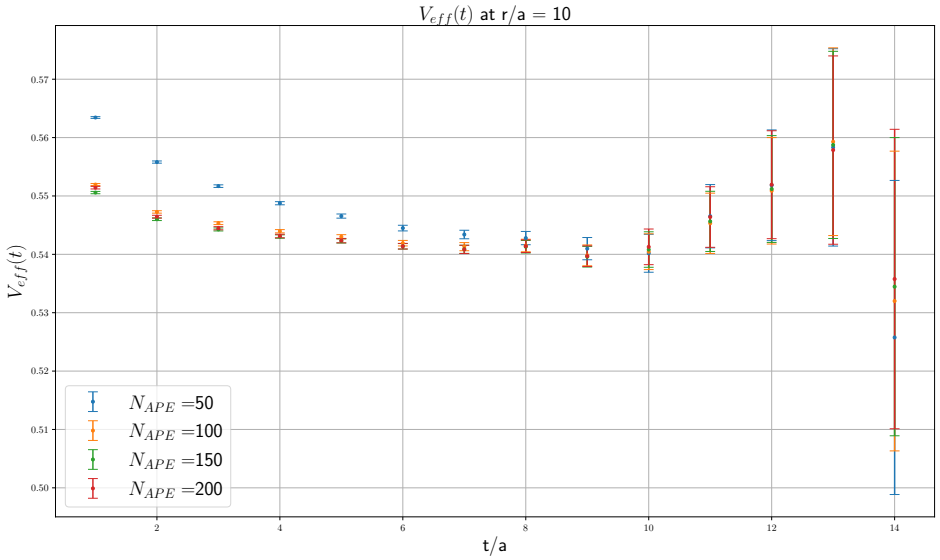

Figure 3.1: $\hat{V}_{\mathrm{eff}}(t)$ at $r/a = 10$ for different numbers of APE-smearing steps, computed without the multilevel algorithm.

Using conventional methods and the multilevel algorithm, Wilson loops have been computed for a number of values of N_{APE}. The results for $r/a = 10$ are shown in figure (3.1). We checked the multilevel results by comparing to conventional computations. Here, conventional results are denoted with index conv, multilevel results with index mlevel. The ratio was for all r and t equal to 1 within errors, an example is given in figure (3.2) for a Wilson loop. Effective potentials $V_{\mathrm{eff}}(r,t)$ were investigated for plateaus, to extract values of the static potential $V_0(r)$. To properly describe the static potential in the small distance region, we used the parametrization from reference [1], which uses an additional $1/r^2$-term, so in total one has

$$V_0(r) = V_c - c_1/r + c_2/r^2 + \kappa r \tag{3.2}$$

The extracted string tension κ and shift V_c for both, multilevel and conventional results,

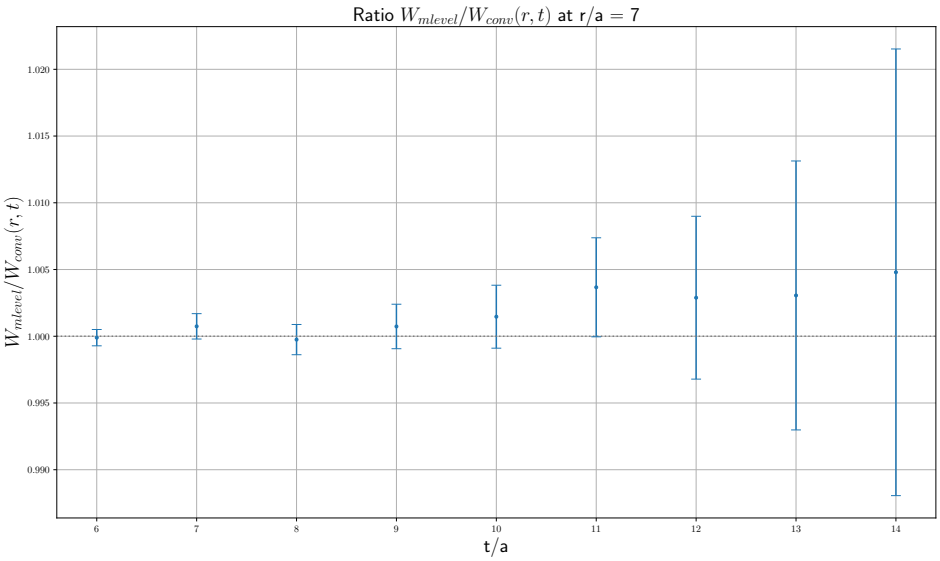

Figure 3.2: Ratio of conventional (conv) and multilevel (mlevel) results for $\langle W \rangle$ at $r/a = 7$.

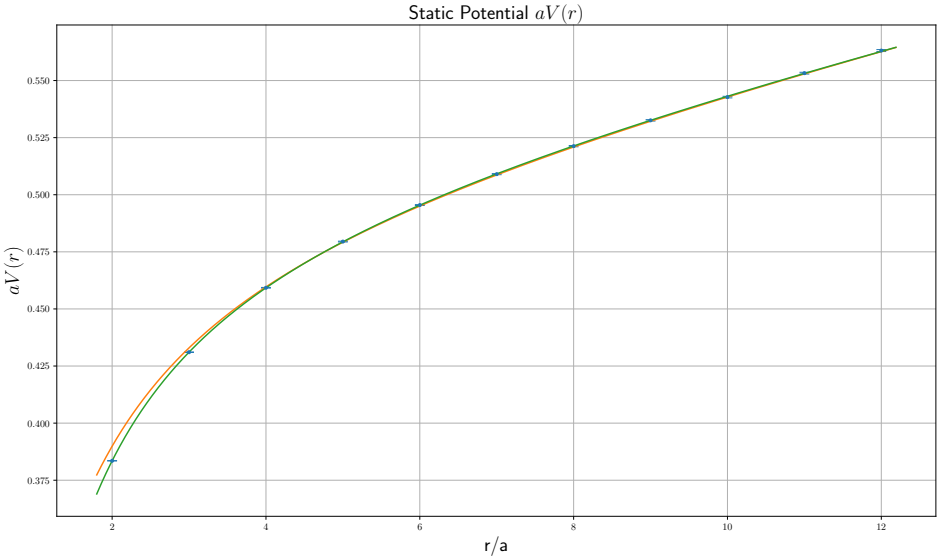

Figure 3.3: $\hat{V}_0(r/a)$ computed without the multilevel algorithm. The lines shown are the fit curve to the data points (green) and the curve using fitparameters from reference [1] (yellow).

at all N_{APE}'s, is equal to the one from reference [1], but c_1 and c_2 are different. The difference can be seen at small distances in figure (3.3). We tried to simulate our Wilson loops with the same set of parameters as in reference [1], the only difference was the application of link integration in this reference. However, it is unlikely that link integration is the source for this deviation, since it is a technique which only reduces statistical noise, but leads to an exact expression. It remains unclear, where this deviation comes from.

The static potential was also computed with Wilson loops results from the multilevel computations. Conventional and multilevel results from our computations are in agreement with each other. The multilevel algorithm led also to slightly improved statistical errors. Figure (3.3) shows the plot for $\hat{V}_0(r/a)$. Table 3.3 shows fitparameters for both computations.

3.3 Correlation Functions

Equations (2.18-2.21) show, how one can compute the spin-potentials from colour field correlation functions. The approach to compute the spin-potentials is to parametrize data points with a suitable ansatz, which can be integrated analytically. This way, parameters from fit curves to our data can be inserted into the analytical expression for each spin-potential (see equations (2.22), (2.23)). In the following, a correlation function $C_i(t)$, $i = 1, 2, 3, 4$ denotes the combination of colour field correlation functions needed to compute the corresponding spin-potential. Equation (2.45) shows the spectral decomposition for our correlation functions in the limit $\Delta t \to \infty$, which is an infinite sum of exponentials. An additional constraint comes for $C_1(t)$ and $C_2(t)$. Due to invariance under time inversion, these two correlators have to vanish at $t = 0$. We discussed in section 2.2, how we can cut off the multi-exponential at $m_{\max}$, in order to fit this ansatz to our results. $m_{\max}$ is chosen, such that χ^2/N_{DF} is of order 1 and fits are stable. Especially at larger distances, a two-exponential fit turned out to be unable to properly describe the data for both, small and large t. Fits were found to be highly unstable and χ^2/N_{DF} was often of order $100 - 1000$. Three exponentials were in much better agreement with the data, with χ^2/N_{DF} being close to 1.0 and only few exceptions. Different sets of initial parameters also did not change the results, which implies that the fits were stable.

Figure (3.4) shows the results for the correlator $C_2(t)$ at $r/a = 4$ with $m_{\max} = 2, 3$. Even though the curves show significant differences in the plot, the resulting values for the potential are roughly equal. What is important for C_1 and C_2 is the behaviour for $t/a \in [5, 10]$, where C_1 and C_2 have non-vanishing contributions. The potentials V_1', V_2' are computed by integrating $t \cdot C_1$, or $t \cdot C_2$ over time, hence contributions in this interval are significant. In this example, both fits coincidentally show similar behaviour for large t, hence the values for V_2' are similar. In most cases, however, a two-exponential fit approaches 0 too soon, cutting off important contributions. This can be seen in figure (3.5). A third exponential with a small exponent and small amplitude is able to compensate for this.

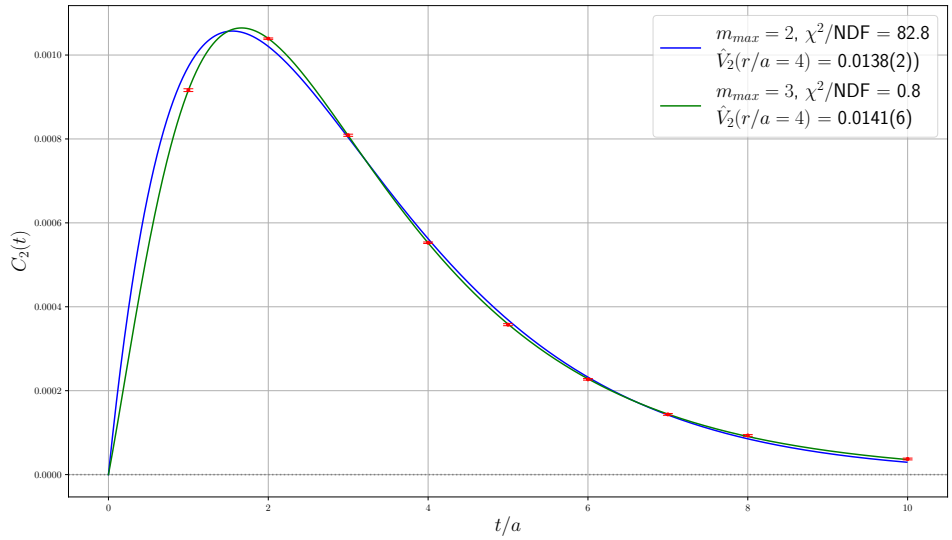

Figure 3.4: Two- and three-exponential fits to the data of $C_2(t)$ at $r/a = 4$. The derived values for $V_2'(r)$ are similar, but the two-exponential fit has a much larger value for χ^2/N_{DF}.

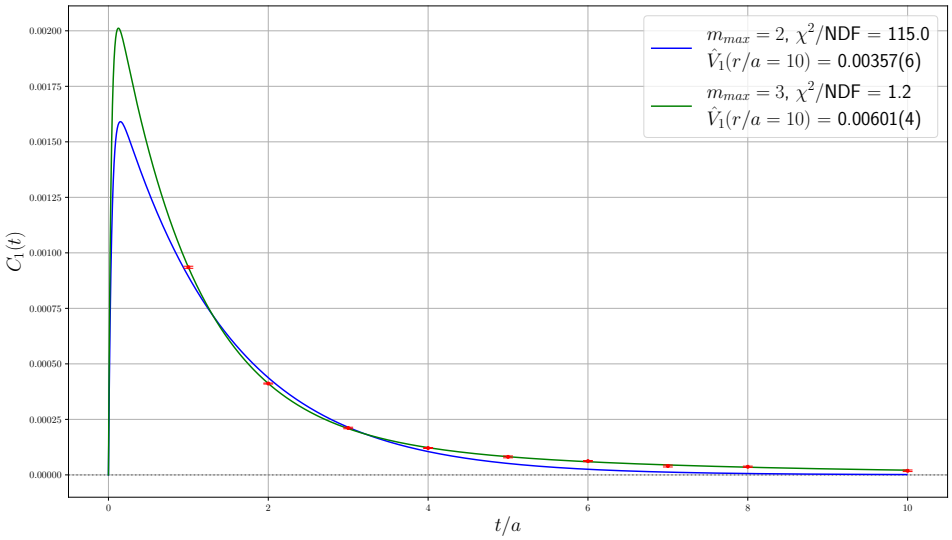

Figure 3.5: Two- and three-exponential fits to the data of $C_1(t)$ at $r/a = 10$. The curve with two exponentials vanishes too soon, cutting off contributions at large t.

We fitted the data for the correlation functions $C_1(t)$, $C_2(t)$, $C_3(t)$ and $C_4(t)$ for all distances from $r/a = 2$ to $r/a = 10$, using a three-exponential fit. Various correlation functions are shown in figures (A.1-A.8) in appendix A. As mentioned above, $C_1(t)$ and

Table 3.4: χ^2/N_{DF} for the three-exponential fits to correlation functions $C_i(t)$.

r/a	χ^2/N_{DF} for	$C_1(t)$	$C_2(t)$	$C_3(t)$	$C_4(t)$
2		0.95	2.94	0.72	0.97
3		0.28	27.30	0.09	0.99
4		1.28	0.79	1.95	0.42
5		0.66	1.12	3.16	1.14
6		0.23	0.87	4.39	1.11
7		0.50	1.19	1.43	1.87
8		1.73	1.50	0.85	0.26
9		1.58	0.39	1.46	1.42
10		1.21	2.06	0.79	1.01

$C_2(t)$ can be shown to vanish at $t = 0$, therefore, we only computed $C_1(t/a \geq 1)$ and $C_2(t/a \geq 1)$. This is not the case for $C_3(t)$ and $C_4(t)$. χ^2/N_{DF} is listed for each correlation function in table 3.4.

Table 3.5: Fitparameters for $V_2'(r) - V_1'(r)$.

Parametrization	$a^2\kappa$	c_1	$a^{-1}c_2$	χ^2/N_{DF}
$\kappa + \frac{c_1}{r^2}$	0.00686(7)	0.236(3)		4.35
$\kappa + \frac{c_1}{r^2} - \frac{2c_2}{r^3}$	0.00628(6)	0.285(3)	0.06(9)	0.58

3.4 Spin-dependent Corrections

In this section, we have finished the integrals from equations (2.18-2.21) and present the results for the spin-dependent potentials.

3.4.1 Gromes Relation

Before presenting the spin potential results, we would like to investigate Gromes' relation $V_0'(r) = V_2'(r) - V_1'(r)$. It is the only exact prediction for the potentials, which holds beyond the short distance regime [10]. V_0' is computed via fitparameters derived from the static potential. Results for $V_2'(r) - V_1'(r)$ deviate from the static force and the derived string tension is noticeably smaller. This can be seen in figure (3.6), table 3.5 shows the derived fitparameters. To make the difference more visible, figure (3.7) shows the ratio for the fit curves $V_2'(r) - V_1'(r)$ and $V_0'(r)$. At $r/a = 10$, the spin-potentials show a difference of more than 10% from the static force. Reference [10] found for the Gromes relation similar results. Discretization can be a possible source for this deviation. On one hand, the relation is derived in the continuum by demanding Lorentz invariance. Reference [10] suggests, that deviations are expected due to a finite cut-off a for relations which are derived in the continuum. In the limit $a \to 0$, Lorentz invariance should be restored. On the other hand, we used a formulation for colour fields which is affected by lattice artefacts. Equation (2.33) makes use of the Taylor expansion of the plaquette in order to define the field-strength tensor. Huntley-Michael renormalization factors led to more accurate expressions for colour fields, but a finite contribution from the lattice cut-off a is still present. The effect of discretization on the Gromes relation should be tested in the continuum limit in future studies.

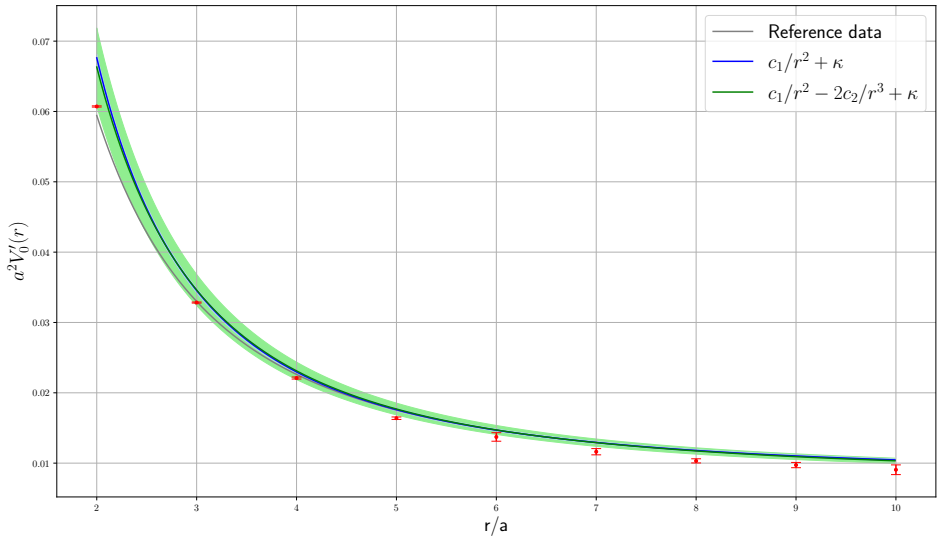

Figure 3.6: Data points for $V_2'(r) - V_1'(r)$ and the static force. For the static force, the two parametrizations are shown, as well as the result from reference [1].

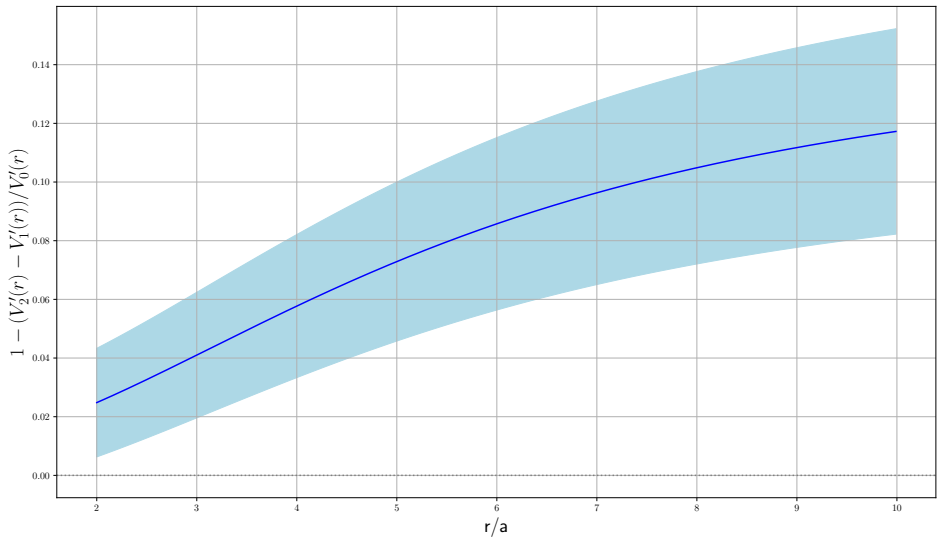

Figure 3.7: Percentaged deviation between the fit for $V_2'(r) - V_1'(r)$ and the static force $V_0'(r)$.

3.4.2 Spin-Potentials

In the following, we will try to find a suitable ansatz for each spin-potential, in order to parametrize them. From perturbation theory, one can derive approximate relations

between the spin potentials V_2', V_3 and V_4 and in total, the shape of each spin-potential. The static potential and the spin-potentials take the following form [1, 10]:

$$V_0(r) = S(r) + V(r) \tag{3.3}$$

$$V_1'(r) = -S'(r) \tag{3.4}$$

$$V_2'(r) = V'(r) \tag{3.5}$$

$$V_3(r) = \frac{V'(r)}{r} - V''(r) \tag{3.6}$$

$$V_4(r) = 2\Delta V(r) \tag{3.7}$$

$$S(r) = \kappa r \tag{3.8}$$

$$V(r) = -\frac{c_1}{r} \tag{3.9}$$

$S(r)$ and $V(r)$ are motivated by the static potential. The static potential and $V_1'(r)$ do not show terms including κ in leading order perturbation theory (i. e. $V_1'(r) = 0$). These terms are added in order to match numerical results for the static potential from lattice QCD. Equations (3.4-3.7) with the given $S(r)$ and $V(r)$ will lead to the expressions from equations (2.27-2.28). Our ansatz for the static potential in section 3.2 included an additional term c_2/r^2, which will also be included in the following discussions. For V_3 and V_4 one also expects further contributions, which are relevant at short distances r [10]:

$$V_3(r) = \frac{V'(r)}{r} - V''(r) + P''(r) - \frac{P'(r)}{r} \tag{3.10}$$

$$V_4(r) = 2\Delta V(r) + \Delta P(r) \tag{3.11}$$

$$P(r) = -g' e^{-m_g r} \tag{3.12}$$

The term $P(r)$ is motivated by the exchange of pseudo-scalar particles.

For a long time, results from numerical computations for spin-potentials were found to be in agreement with equations (3.4-3.7) [1, 10]. However, precise computations in $SU(3)$ from reference [10] found deviations from these expectations. In particular, $V_2'(r)$ does not seem to vanish for $r \to \infty$ and $-V_1'(r)$, which should be equal to the string tension, is smaller than expected. This is what we will investigate in the following. Fit results for all investigated parametrizations can be found in table 3.6.

The expectation for the potential $V_1'(r)$ is, that it is constant $-\kappa$. Reference [10] suggests

that data points at $r/a = 2$ are affected by lattice artefacts. We took this into account and performed the fits in the regions $r/a \geq 3$. The derived string tension, however, is different from the one derived from the Gromes relation, as well as the static force. In total, we do not find the data consistent with a constant value within our accuracy. Though this result contradicts the expectation, it is in agreement with a result from reference [1], where $V_1'(r)$ was not found to be constant either. Approaching this in a similar way to reference [1], by adding a term c_1/r^2 to our ansatz, is more consistent with our data, but performed fits come with a large χ^2/N_{DF}. This is shown in figure (3.8). Adding yet another term from the static force, $-2c_2/r^3$, allows to also include the point at $r/a = 2$. For consistency, in the shown fit the point at $r/a = 2$ was omitted. The parameter κ from the fit to $V_1'(r)$ is not in agreement with the one derived from the static force $V_0'(r)$, or the Gromes relation $V_2'(r) - V_1'(r)$. Since this suggests, that κ from our ansatz for $V_1'(r)$ is not the same κ as in our ansatz for $V_2'(r) - V_1'(r)$, we will for now denote all fit parameters with an index corresponding to the respective potential (e. g. $\kappa_{v1}, c_{1,v1}, c_{2,v2}$ for $V_1'(r)$).

Figure (3.9) shows the results for $V_2'(r)$. We found the potential to approach a constant for large r and included a term κ_{v2} in our ansatz. Similar to $V_1'(r)$, we also included a term $-2c_{2,v2}/r^3$. This parametrization is able to describe the data at $r/a = 2$, even though it was omitted in the fit range. The parameters c_1 and c_2 here were smaller than the parameters extracted from the static force and Gromes relation. Nevertheless, the sum of the respective parameters are within errors consistent with the Gromes relation, i. e.

$$\kappa_{\mathrm{Gromes}} = \kappa_{v1} + \kappa_{v2} \tag{3.13}$$

$$c_{1,\mathrm{Gromes}} = c_{1,v1} + c_{1,v2} \tag{3.14}$$

$$c_{2,\mathrm{Gromes}} = c_{2,v1} + c_{2,v2} \tag{3.15}$$

One fitparameter can compensate for deviations of other fitparameters within statistic accuracy. Therefore, in general, parameters from two separate fits are not necessarily similar to parameters from the combined fit, like V_1', V_2' and $V_2' - V_1'$ here. However, the fitparameters from table 3.5 (Gromes relation) and table 3.6 (V_1', V_2') are in good agreement with each other. This suggests that constant and $1/r^2$-contributions mix in V_1' and V_2', where the constant part dominates in V_1' and the $1/r^2$-part in V_2'. We also tested

the effective ansatz from reference [10], $V_2'(r) = \kappa + c'/r^p$ with free parameters c' and p. The resulting curve is identical to our ansatz within errors inside the respective fit range.

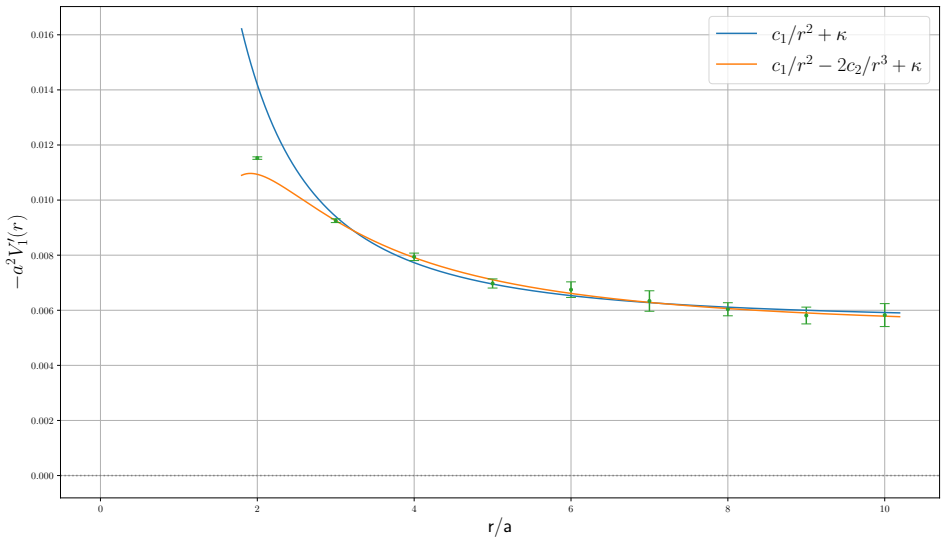

Figure 3.8: Results for $V_1'(r)$, fit curves include linear, $1/r^2$ and $1/r^3$-contributions.

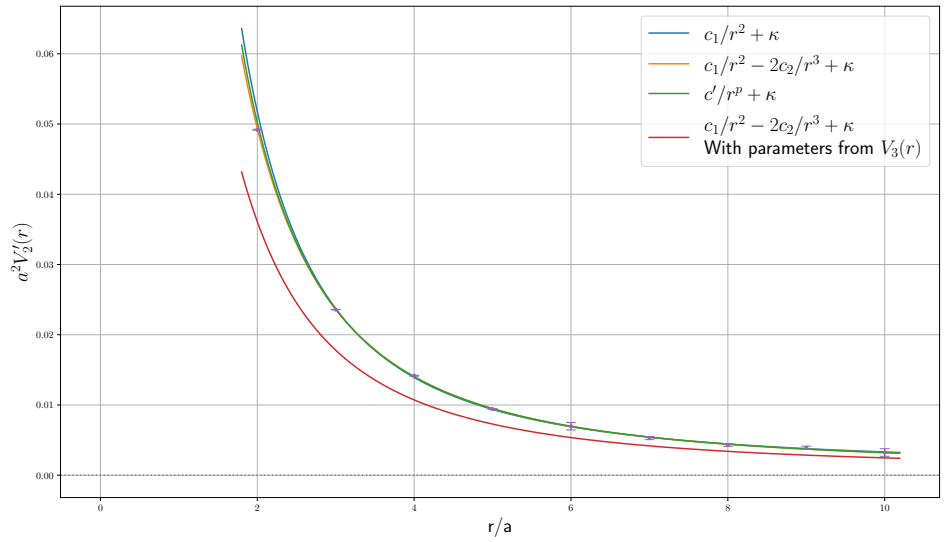

Figure 3.9: Same as figure (3.8) with $V_2'(r)$. An additional curve, which is covered almost entirely the yellow curve, shows the effective parametrization used in reference [10]. The red curve presents a parametrization using fit parameters from $V_3(r)$.

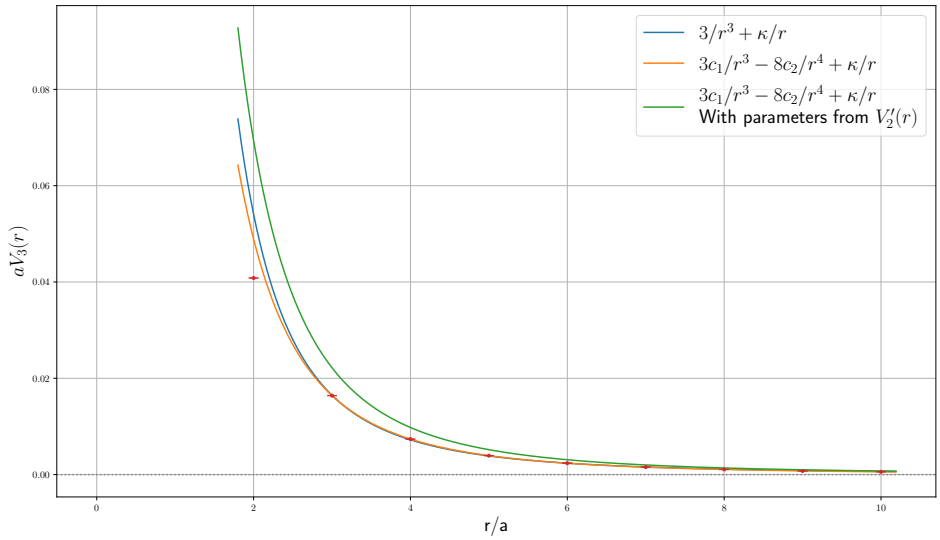

Figure 3.10: Results for $V_3(r)$, with fit curves that include vector and scalar contributions, but neglects pseudo-scalars. The yellow line shows results for the effective parametrization used in reference [10] for a fit range including $r/a = 2$. The green curve presents a parametrization using fit parameters from $V_2'(r)$.

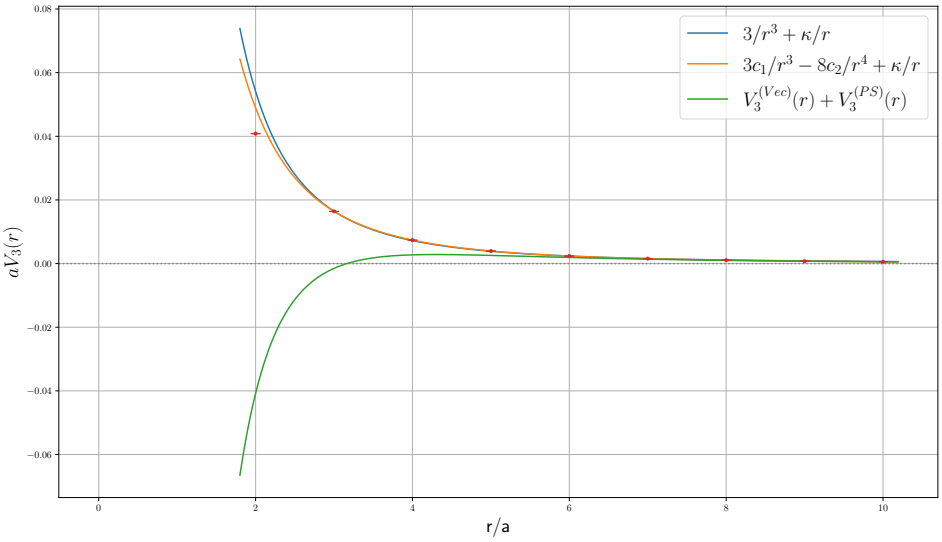

Figure 3.11: Same plot as figure (3.10) with a parametrization $V_3^{\mathrm{Vec}}(r) + V_3^{\mathrm{PS}}(r)$ according to equation (3.16). The parameters for this curve were derived from $V_4(r)$, except c_1 which is derived from the static potential $V_1(r)$.

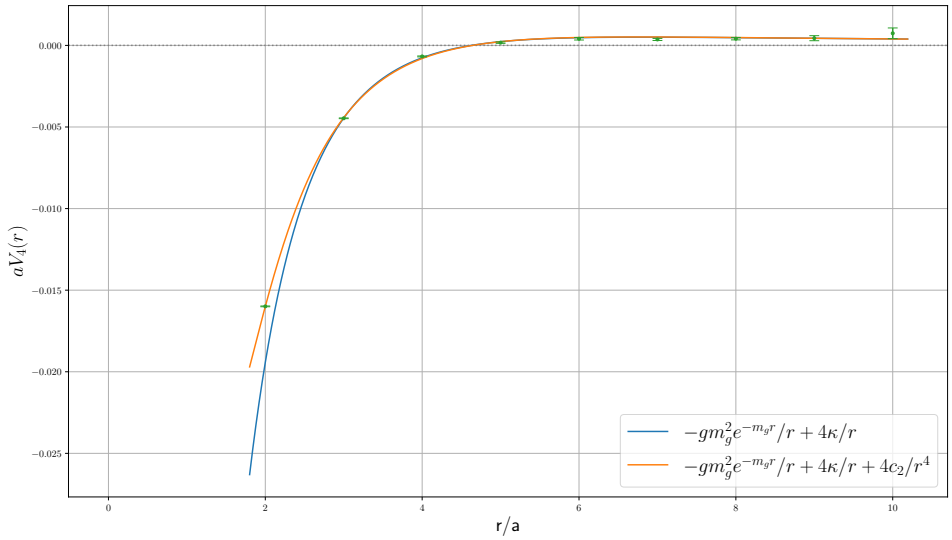

Figure 3.12: Results for $V_4'(r)$, fit curves include vector, as well as pseudo-scalar contributions.

Our results for $V_3(r)$ are shown in figure (3.10). The relation $V_3(r) = \frac{V'(r)}{r} - V''(r)$ is modified to include a possible constant in $V_2'(r)$. We also tested the effective parametrization used in reference [10], $V_3(r) = c'/r^p$ with free parameters c' and p. Again, the curves show identical results within the fit range $r/a \in [3, 10]$. Even though the results for both parametrizations are very similar, χ^2/N_{DF} is much higher for the effective parametrization. χ^2/N_{DF} assumes high values, when including $r/a = 2$, but it is not clear, if the problem is lattice artefacts, which affect our data, or a bad parametrization. Furthermore, one can investigate $V_3(r)$ for a possible additional contribution, which can be seen in equation (3.10). In this case, we would have

$$\begin{aligned} V_3(r) &= V_3^{\mathrm{Vec}}(r) + V_3^{\mathrm{PS}}(r) \\ &= \frac{\kappa_{v3}}{r} + 3\frac{c_{1,v3}}{r^3} - 8\frac{c_{2,v3}}{r^4} \\ &\quad - g'(m_g^2 r^2 + 3m_g r + 3)\frac{e^{-m_g r}}{r^3} \end{aligned} \tag{3.16}$$

This ansatz requires a large number of fit parameters and did not provide a stable fit for our data. However, an additional term like this would lower the value of V_3 at small distances r and presumably cover the data point at $r/a = 2$. Reference [10], which suggested

this term, plotted $V_3^{\mathrm{Vec}}(r)$ and $V_3^{\mathrm{PS}}(r)$ with g', m_g and κ (there it is σ) from the fit to $V_4(r)$ and c_1 taken from the static potential $V_0(r)$. There, the resulting curve $V_3^{\mathrm{Vec}}(r) + V_3^{\mathrm{PS}}(r)$ was in good agreement with all shown data points, in particular those at small r. We tested this parametrization as well, with parameters from $V_4(r)$ (c_1 from $V_0(r)$). The result is shown in figure (3.11). Unfortunately, the chosen parameters were not sufficient to describe the data. Nevertheless, this does not contradict a behaviour according to equation (3.16). It is interesting to see in future studies, which results a more detailed investigation of $V_3(r)$ for a possible contribution $V_3^{\mathrm{PS}}(r)$ can bring.
For $V_4(r)$, the expected result under negligence of pseudo-scalar contributions was a delta function and older studies confirmed this within accuracy [1]. Preciser measurements nevertheless have found for larger r, that a delta function and also a pseudo-scalar correction was not sufficient, to describe the data. Reference [10] found again, that including a term which corresponds to the finite tail in $V_2'(r)$ was able to handle this problem. Our results can be found in figure (3.12). Without $r/a = 2$, this was a suitable parametrization. We also tried to include the c_2/r^2-term from $V_2'(r)$, which resulted in a parametrization which could cover the point at $r/a = 2$. In both cases, κ_{v4}, g' and m_g were equal within errors.

The parametrizations for the spin-dependent potentials we discussed are motivated by perturbative computations and we had to modify them, in order to be in agreement with our data. . The respective sets of parameters for V_2', V_3 and V_4 do not necessarily have to be identical, since deviations in one parameter between the potentials can be compensated by other parameters. To cross-check our parametrizations and results, we applied fit parameters from one potential to curves from other potentials. In particular for V_3, we found that parameters extracted from V_2' are not suitable to describe the data points and vice versa. This can be seen in figures (3.9,3.10), where the respective curve is shown. It is unclear, if this difference is due to a bad fit, or due to other error sources, e. g. discretization. Equation (2.24) is also not an exact relation, but derived in perturbation theory and leaves space for deviations. For future works, this finding has to be revisited in order to find a definitive answer.

Table 3.6: Spin-potential fit parameters for different parametrizations.

Potential	Fit range (r/a)	Parametrization, parameters	$\chi^2/N_{\rm DF}$
$-V_1'(r)$		$\kappa_{v1} + \frac{c_{1,v1}}{r^2}$	
	$3-10$	$a^2\kappa_{v1} = 0.00557(3),\ c_{1,v1} = 0.0344(7)$	1.42
		$\kappa_{v1} + \frac{c_{1,v1}}{r^2} - 2\frac{c_{2,v1}}{r^3}$	
	$3-10$	$a^2\kappa_{v1} = 0.00523(7),\ c_{1,v1} = 0.062(8),$	0.22
		$a^{-1}c_{2,v1} = 0.04(0)$	
$V_2'(r)$		$\kappa_{v2} + \frac{c_{1,v2}}{r^2}$	
	$3-10$	$a^2\kappa_{v2} = 0.00129(4),\ c_{1,v2} = 0.201(8)$	6.20
		$\kappa_{v2} + \frac{c_{1,v2}}{r^2} - 2\frac{c_{2,v2}}{r^3}$	
	$3-10$	$a^2\kappa_{v2} = 0.00104(9),\ c_{1,v2} = 0.222(5),$	1.44
		$a^{-1}c_{2,v2} = 0.02(9)$	
		$\kappa_{v2} + \frac{c'}{r^p}$	
	$3-10$	$a^2\kappa_{v2} = 0.00095(4)\ a^{p-2}c' = 0.185(8),$	1.93
		$p = 1.9(1)$	
$V_3(r)$		$\frac{\kappa_{v3}}{r} + 3\frac{c_{1,v3}}{r^3}$	
	$3-10$	$a^2\kappa_{v3} = 0.00243(5),\ c_{1,v3} = 0.140(9)$	20.60
		$\frac{\kappa_{v3}}{r} + 3\frac{c_{1,v3}}{r^3} - 8\frac{c_{2,v3}}{r^4}$	
	$3-10$	$a^2\kappa_{v3} = 0.00077(0),\ c_{1,v3} = 0.177(0),$	0.33
		$a^{-1}c_{2,v3} = 0.03(5)$	
$V_4(r)$		$\frac{\kappa_{v4}}{r} - g'm_g^2\frac{e^{-m_g r}}{r}$	
	$3-10$	$a^2\kappa_{v4} = 0.00099(7),$	6.87
		$g' = 0.31(9),\ am_g = 0.9(0)$	
		$\frac{\kappa_{v4}}{r} + \frac{4c_{2,v4}}{r^4} - g'm_g^2\frac{e^{-m_g r}}{r}$	
	$2-10$	$a^2\kappa_{v4} = 0.00095(9),\ a^{-1}c_{2,v4} = 0.03(8),$	4.44
		$g' = 0.41(1),\ am_g = 0.8(8)$	

Chapter 4

Conclusions

4.1 Summary

We computed the static potential and spin-dependent corrections in $SU(2)$, using the multilevel algorithm for Wilson loops. Comparison has shown, that results computed using the multilevel algorithm are equal to results from conventional methods. Wilson loops at intermediate distances and large t have shown an error reduction of factor 10, with an increase in computational effort of 40 sublattice updates $N_c^{(1)}$. In particular, correlation functions at large r, t could be accessed in a much more effective way. Since spatial lines of loops were placed on fixed boundaries, APE-smearing was only needed on the global configurations, which also reduced the computational effort. The multilevel algorithm has therefore proven itself to be well applicable on Wilson loops.

The required correlation functions were computed with high accuracy and led to stable fits for distances up to $r/a = 10$. From fit parameters, the spin-dependent potentials were computed and parametrizations, as well as the Gromes relation were tested. The Gromes relation deviated by ten percent, which might be due to discretization. Similar to reference [10], we found, that the expected parametrizations in equations (2.27-2.28) were not sufficient to describe all results. V_1' and V_2' were found to be a mix of a $1/r$-term and a constant, with one contribution dominating respectively. For $V_3(r)$, we found that the ansatz derived from identities involving V_2' is sufficient to describe the data, when one

includes a constant contribution in V_2'. However, inserting parameters derived from V_2' into the ansatz for V_3 does not properly describe our results for V_3 and vice versa. It is suspected, that V_3 also contains an additional pseudo-scalar contribution, which could not be properly tested here due to the large number of parameters and the low number of data points to fit. Testing this ansatz with parameters derived from $V_4(r)$ and the static potential $V_0(r)$ was not in agreement with the data points of $V_3(r)$. Finally, potential V_4, which was expected to result in a delta function, was found to have additional contributions which are in agreement with finite tail of V_2' and exchange of pseudo-scalars.
In total, a statistically more precise computation of the results from reference [1] led to the same findings in $SU(2)$, as in reference [10] for $SU(3)$.

4.2 Outlook

Studies on exotic particles, such as hybrid mesons and tetra quarks, rely on an accurate descriptions of heavy quark potentials. Reference [6] studied heavy-light meson decay channels in the Born-Oppenheimer approximation, using the static potential from lattice QCD for heavy quarks. Further studies on systems with bottom and light quarks are given in reference [7]. Both references expect improvements from relativistic corrections, such that preciser computations can be performed and e. g. excited meson-meson channels can be studied. Improvements have already been achieved in $SU(3)$ with corrections at order $\mathcal{O}(m^{-1})$ and spin-dependent corrections at $\mathcal{O}(m^{-2})$ (see reference [9, 14]). Spin-independent corrections, however, remain mostly unexplored. Furthermore, it will be interesting to see, if a combination of all relativistic corrections to order $\mathcal{O}(m^{-2})$ would give accurate results for BO-computations involving charm quarks. Concerning colour field correlation functions, large discretization errors could still be present, since methods like the HM-renormalization are only a perturbative approach. An improved solution to this problem is desirable. Reference [16] provides a discussion on this topic focusing on electric fields.

Appendices

Appendix A

Correlation Function Plots

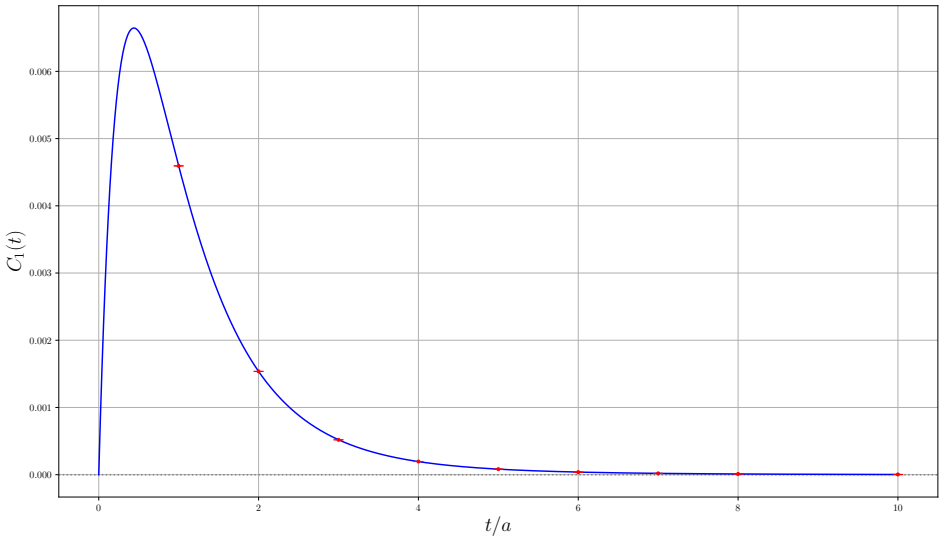

Figure A.1: $C_1(t)$ at $r/a = 2$. The blue line is the fit curve, which uses the ansatz from equation (2.45) with cut-off $m_max = 3$.

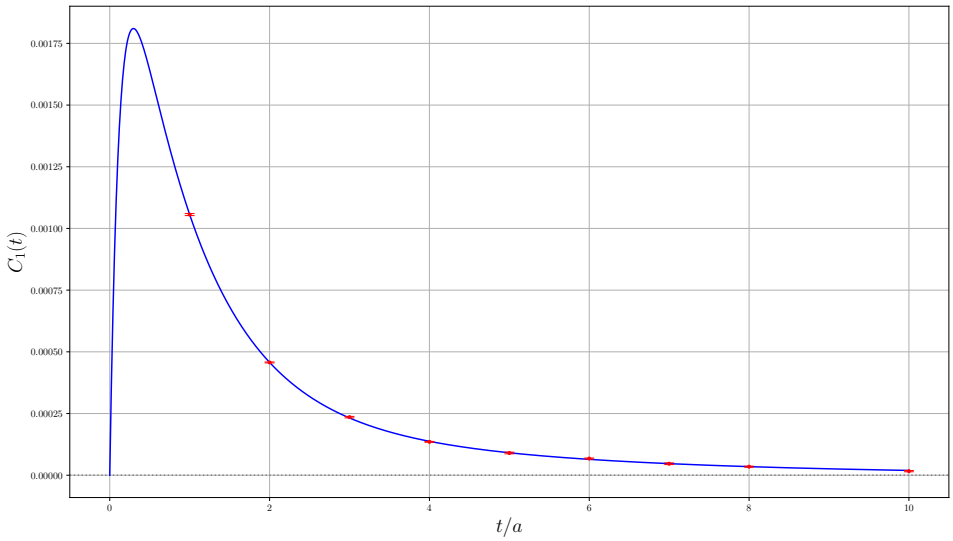

Figure A.2: Same plot as in figure (A.1) at $r/a = 8$.

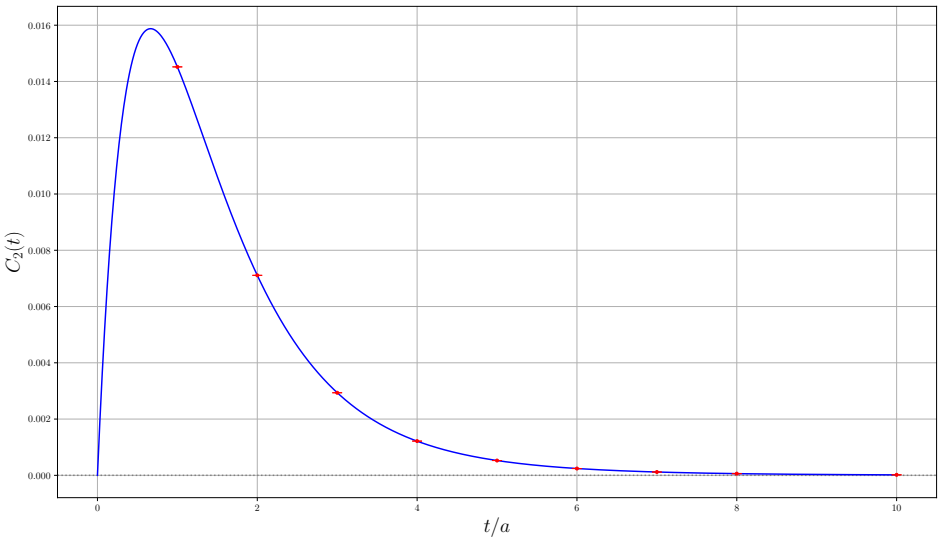

Figure A.3: Same plot as in figure (A.1) with $C_2(t)$ at $r/a = 2$.

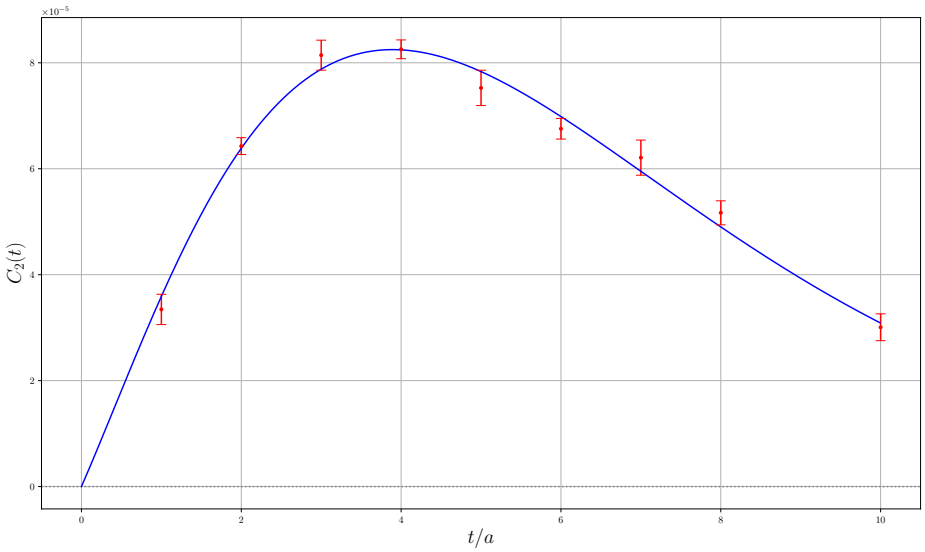

Figure A.4: Same plot as in figure (A.3) at $r/a = 8$.

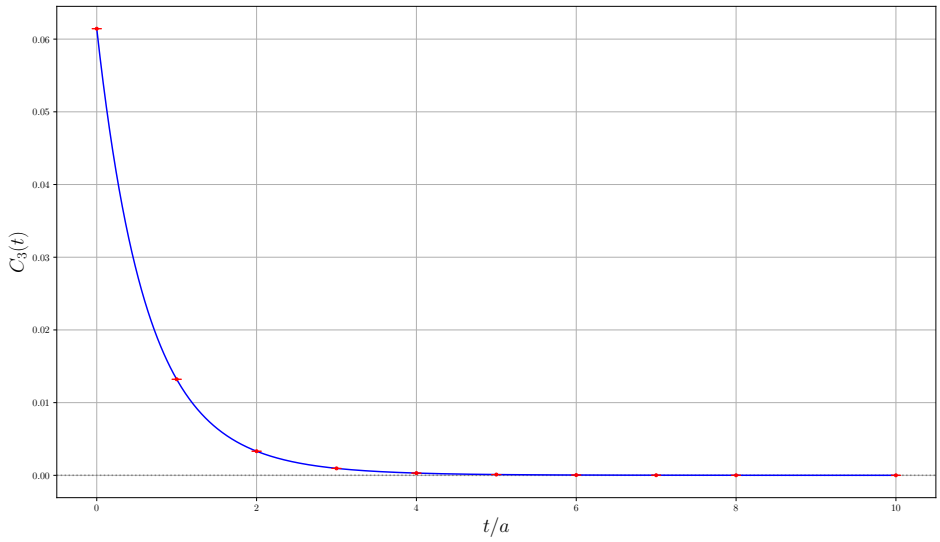

Figure A.5: Same plot as in figure (A.1) with $C_3(t)$ at $r/a = 2$.

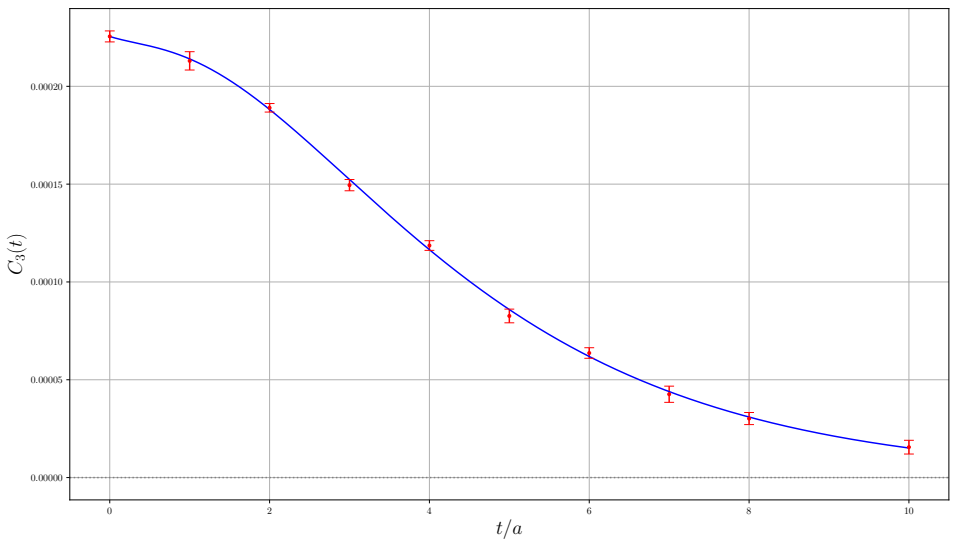

Figure A.6: Same plot as in figure (A.5) at $r/a = 8$.

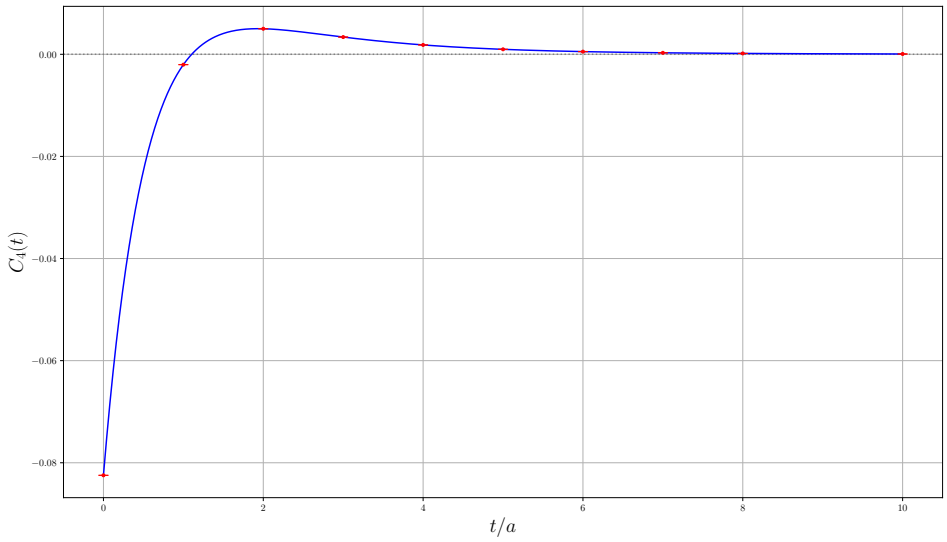

Figure A.7: Same plot as in figure (A.1) with $C_4(t)$ at $r/a = 2$.

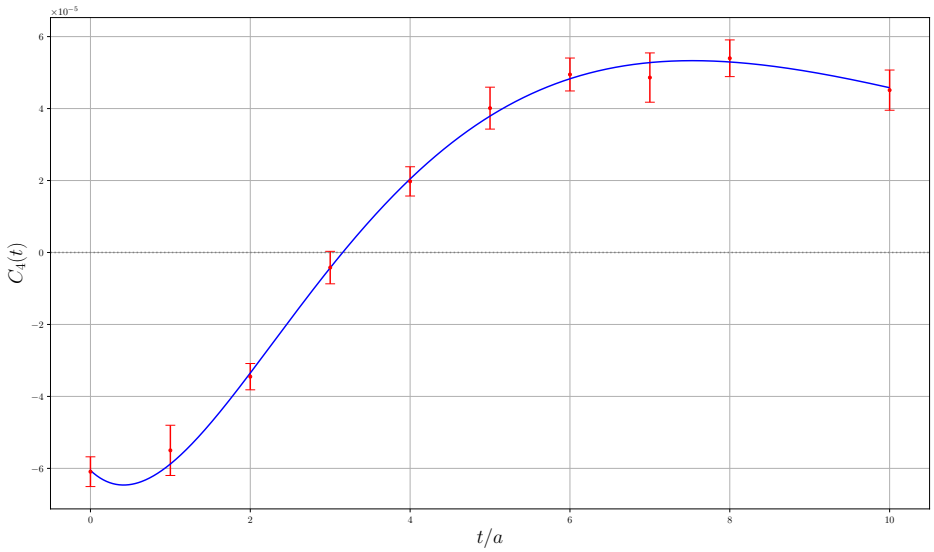

Figure A.8: Same plot as in figure (A.7) at $r/a = 8$.

Acknowledgements

I want to thank Professor Marc Wagner for his great supervision. He found a good topic for my thesis and helped me a lot during my studies and research. With the outbreak of COVID-19 and the still ongoing restrictions, communication with people you don't see on a regular basis can be hard. Professor Wagner answered e-mails very fast and often offered appointments to talk on the same, or the next day. The discussions were interesting and I could learn a lot from it. With this, I gained a lot of experience in my last year as a master student and I look forward to becoming a P. h. D. student.

I also want to thank Christian Reisinger, a former P. h. D. student in Professor Wagner's group. Christians studies laid the ground for my thesis. He started to work on the spin-dependent potentials before me and introduced me to the theory and technical details behind it. The programs he coded were also an important part of my work and gave me many insights into numerical physics and coding.

Bibliography

[1] Gunnar S. Bali, Klaus Schilling, and Armin Wachter. Ab initio calculation of relativistic corrections to the static interquark potential. 1: SU(2) gauge theory. *Phys. Rev. D*, 55:5309–5324, 1997. [hep-lat/9611025].

[2] E. Eichten and F. Feinberg. Spin Dependent Forces in QCD. *Phys. Rev. D*, 23:2724, 1981.

[3] Dieter Gromes. Spin Dependent Potentials in QCD and the Correct Long Range Spin Orbit Term. *Z. Phys. C*, 26:401, 1984.

[4] A. Barchielli, E. Montaldi, and G. M. Prosperi. On a Systematic Derivation of the Quark - Anti-quark Potential. *Nucl. Phys. B*, 296:625, 1988. [Erratum: Nucl.Phys.B 303, 752 (1988)].

[5] Nora Brambilla, Antonio Pineda, Joan Soto, and Antonio Vairo. The QCD potential at O(1/m). *Phys. Rev. D*, 63:014023, 2001. [hep-ph/0002250].

[6] Pedro Bicudo, Marco Cardoso, Nuno Cardoso, and Marc Wagner. Bottomonium resonances with $I = 0$ from lattice QCD correlation functions with static and light quarks. *Phys. Rev. D*, 101(3):034503, 2020. [1910.04827].

[7] Pedro Bicudo, Nuno Cardoso, Lasse Müller, and Marc Wagner. Computation of the quarkonium and meson-meson composition of the $\Upsilon(nS)$ states and of the new $\Upsilon(10753)$ Belle resonance from lattice QCD static potentials. *Phys. Rev. D*, 103(7):074507, 2021. [2008.05605].

[8] N. Brambilla. Effective Field Theories and Lattice QCD for the X Y Z frontier, 2021. 38th International Symposium on Lattice Field Theory.

[9] Yoshiaki Koma and Miho Koma. Heavy quarkonium spectroscopy in pNRQCD with lattice QCD input. *PoS*, LATTICE2012:140, 2012. [1211.6795].

[10] Yoshiaki Koma and Miho Koma. Spin-dependent potentials from lattice QCD. *Nucl. Phys. B*, 769:79–107, 2007. [hep-lat/0609078].

[11] Yoshiaki Koma, Miho Koma, and Hartmut Wittig. Nonperturbative determination of the QCD potential at O(1/m). *Phys. Rev. Lett.*, 97:122003, 2006. [hep-lat/0607009].

[12] Martin Luscher and Peter Weisz. Locality and exponential error reduction in numerical lattice gauge theory. *JHEP*, 09:010, 2001. [hep-lat/0108014].

[13] Christof Gattringer and Christian B. Lang. *Quantum chromodynamics on the lattice*, volume 788. Springer, Berlin, 2010.

[14] Yoshiaki Koma and Miho Koma. Scaling study of the relativistic corrections to the static potential. *PoS*, LAT2009:122, 2009. [0911.3204].

[15] Peter Young. Everything you wanted to know about Data Analysis and Fitting but were afraid to ask. *arXiv e-prints*, page arXiv:1210.3781, October 2012. [1210.3781].

[16] Nora Brambilla, Viljami Leino, Owe Philipsen, Christian Reisinger, Antonio Vairo, and Marc Wagner. Lattice gauge theory computation of the static force. 6 2021. [2106.01794].